Up to 1% Pb isotope disequilibrium between minerals hosted in dacites from the Guagua Pichincha volcano, Ecuador: Implication for tracing the source and crustal history of continental arc magmas

Marie-Anne Ancellin, Ivan Vlastélic, Pablo Samaniego, François Nauret, Abdelmouhcine Gannoun, Silvana Hidalgo

Up to 1% Pb isotope disequilibrium between minerals hosted in dacites from the Guagua Pichincha volcano, Ecuador: Implication for tracing the source and crustal history of continental arc magmas

Marie-Anne Ancellin[a,c], Ivan Vlastélic[a], Pablo Samaniego[a], François Nauret[a], Abdelmouhcine Gannoun[a], Silvana Hidalgo[b]

[a] Université Clermont Auvergne, CNRS, IRD, OPGC, Laboratoire Magmas et Volcans, F-63000 Clermont-Ferrand, France
[b] Instituto Geofísico — Escuela Politécnica Nacional, Ladrón de Guevara E11-253 y Andalucía, 6to piso ed. Ing. Civil, Quito, Ecuador
[c] Current address: Institute of Earth Sciences, University of Iceland, Sturlugata 7, 101 Reykjavik, Iceland

Corresponding author: Marie-Anne Ancellin, ancellin@hi.is
Ivan Vlastélic: I.Vlastelic@opgc.univ-bpclermont.fr ; Pablo Samaniego: pablo.samaniego@ird.fr ; François Nauret: Francois.Nauret@uca.fr ; Abdelmouhcine Gannoun: abdelmouhcine.gannoun@uca.fr ; Silvana Hidalgo: shidalgo@igepn.edu.ec

Word count:
Abstract: 357
Text body (without Figure captions): 5641

Keywords: single mineral Pb isotopes, crustal evolution of magmas, primitive melt, Ecuador, Pichincha volcano

ABSTRACT

Continental arc lavas display geochemical signatures that reflect both mantle metasomatism by slab fluids or melts and extensive differentiation of magmas within crustal reservoirs. The relative effect of source and crustal processes are difficult to disentangle based on whole-rock compositions. This issue is critical in Ecuador where volcanism occurs through a thick continental crust (>50 km). This study reconstructs the history of melts feeding the Guagua Pichincha volcano, Western Cordillera, by analysing the Pb isotope composition and major-trace element content of individual minerals (33 amphiboles, 4 orthopyroxenes and 18 plagioclases) hosted in two dacite samples. It uses a low-blank wet-chemistry method for precise analysis of Pb amounts as low as 150 pg.

Early crystallized, high-Al amphiboles with $Al_2O_3 \geq 9.8$ wt.% and Eu/Eu*>0.7 have the lowest and most heterogeneous $^{206}Pb/^{204}Pb$ (18.816-18.999), whereas plagioclases have the highest and most homogeneous $^{206}Pb/^{204}Pb$ (19.003-19.023). Low-Al amphiboles and orthopyroxenes display intermediate compositions and variability (18.934-19.007). The $^{206}Pb/^{204}Pb$ ratio correlates negatively with Eu/Eu* in amphiboles and orthopyroxenes, which indicates that the Guagua Pichincha magmas assimilate radiogenic Pb within the stability field of plagioclase (i.e. in the upper crust). The radiogenic ankaramites of the Guaranda unit, an accreted ocean terrain making the basement of the Western Cordillera, are the most suitable contaminant. If this is correct, the $^{206}Pb/^{204}Pb$ increase from the two most primitive amphiboles to their respective host rocks requires *ca.* 20% crustal assimilation, which is higher than previous estimates in the Northern Volcanic Zone but similar to those inferred for Central Andean mafic lavas. The two most primitive amphiboles with no significant Eu anomaly record the composition of melts before plagioclase crystallization. These deep melts have contrasted

51 $^{206}Pb/^{204}Pb$ ratios (18.816 -18.879) and contents of fluid mobile elements (Li, Cu, Rb, Pb) that
52 probably reflect the input of different slab components to the mantle wedge. Melts in equilibrium
53 with the two most primitive amphiboles of the Guagua Pichincha volcano are enriched in
54 incompatible elements, but depleted in fluid mobile elements compared to the olivine-hosted
55 melt inclusions of the older Rucu Pichincha volcano. This supports previous inferences based on
56 whole-rock data that the mantle source of the Pichincha Volcanic Complex has changed through
57 time.
58

1. Introduction

Arc magmas display a much larger compositional variability than those generated at ocean ridges or intraplate volcanism. Such heterogeneity reflects variations in the nature and amount of subducted material along with the geodynamics and thermal state of the arc system (e.g. Gill, 1981; Hawkesworth et al., 1993; Turner et al., 2016), and the variable contamination of mantle-derived melts within the arc crust (e.g. Taylor, 1980; Hildreth and Moorbath 1988; Annen et al., 2006). Indeed, the crustal filter generally blurs the chemical and isotopic signature of mantle melts, hampering the study of subduction processes. This issue is particularly important in continental arc settings where thick crust promotes extensive modification of mantle magmas (Hildreth and Moorbath, 1988; Annen et al., 2006; Mantle and Collins, 2008; Farner and Lee, 2017). Primitive melt compositions are conventionally measured in melt inclusions hosted in early crystallizing minerals (Sobolev, 1996; Schiano, 2003). However, accurately measuring radiogenic isotopes in melt inclusions remains a very challenging task (Paul et al., 2011; Rose-Koga et al., 2012; Reinhard et al., 2018) and sufficiently large melt inclusions are absent in many arc eruptive products. Hence, geochemists lack an unequivocal method to discriminate slab, mantle and crustal components in arc magmas.

In Ecuador, this issue is critical as the continental crust thickness exceeds 50 km (Guillier et al., 2001; Vaca et al., 2019), resulting in the scarcity of primitive compositions in bulk eruption products (Monzier et al., 1999; Hidalgo et al., 2012; Ancellin et al., 2017) and the rare occurrence of olivine-hosted melt inclusions (Le Voyer et al., 2008; Narváez et al., 2018). In such a situation, this study attempts to trace the source and crustal history of Ecuador arc magmas from the Pb isotopic composition of minerals. To this end, we have developed a wet–chemistry method for measuring precisely the isotope composition of small Pb amounts (Pb >

0,15 ng). We use this method to analyse single minerals hosted in hand-sized samples from Guagua Pichincha, the youngest edifice of the long-lived Pichincha volcanic complex (Western Cordillera, Ecuadorian Andes) (Samaniego et al., 2010). Analysing both early and late crystallizing minerals allows us to reconstruct the Pb isotope evolution of melts within the crust, and to constrain the composition of the primitive melts. The data are used to disentangle the signature of the magma source from the effects of crustal contamination, and to discuss the origin of the elevated ratios of heavy to light Rare Earth Elements that generally characterize frontal arc volcanoes. The large Pb isotope heterogeneity of minerals also raises questions on the significance of the bulk isotopic composition of extensively crystallized rocks commonly produced in continental arcs, and their relevance for tracking changes in the magma source.

2. Geological setting and main scientific goal

The Ecuadorian arc is part of the Northern Volcanic Zone of the Andes. It results from the subduction of the Nazca plate below the South American continent, at a rate of 55-60 mm/year (Trenkamp et al., 2002, Nocquet et al., 2014). The main part of the arc developed in front of the Carnegie ridge, which is the track of Galápagos hotspot activity on the Nazca plate (Fig. 1). In Ecuador, the arc is composed of the Western and the Eastern Cordilleras separated by the Interandean valley. It roughly includes 84 Quaternary volcanic edifices that lie upon a ~50 km-thick crust for the most, apart from back-arc volcanoes which rest upon a 30-40 km-thick crust (Feininger and Seguin, 1983; Guillier et al., 2001; Vaca et al., 2019).

The Pichincha Volcanic Complex is located in the Western Cordillera a few kilometres to the west of Quito (Fig. 1). It rests on oceanic terrains accreted between the late Cretaceous and the Palaeogene (Mamberti et al., 2003; Jaillard et al., 2004, 2008). The volcanic complex

105 includes the old Rucu Pichincha volcano, which erupted mostly andesites between 1.1 and 0.15
106 Ma, and the Guagua Pichincha volcano that erupted mainly dacites since 60 ka (Robin et al.,
107 2010). During the Rucu Pichincha to Guagua Pichincha transition, ratios of trace elements that
108 are more *vs.* less incompatible (e.g. Th/La, La/Yb) increased, whereas fluid-mobile to fluid-
109 immobile element ratios (e.g. Ba/Th, B/Th) decreased, which led Samaniego et al. (2010) to
110 suggest that the metasomatic agent evolved from a hydrous-fluid to a siliceous-melt. These
111 authors linked the evolution from slab dehydration to slab partial melting to an increasing
112 geothermal gradient during the subduction of the Carnegie Ridge. This model assumes that
113 crustal processing of Pichincha magmas is a second order process, which is supported by the
114 small variations of whole-rock $^{87}Sr/^{86}Sr$ (0.70396–0.70412), $^{143}Nd/^{144}Nd$ (0.51286–0.51293) and
115 $\delta^{18}O$ (7.5-7.8‰) (Samaniego et al., 2010; Hidalgo et al., 2012). On the other hand, Chiaradia et
116 al. (2009) observed some correlation between the small Pb and Sr isotopic variations and
117 evolution indices (e.g. CaO, K_2O). These authors emphasized the importance of crustal
118 contamination of Pichincha magmas, and more generally, suggested that high La/Yb and Sr/Y
119 ratios of frontal arc volcanoes first reflect magma evolution and crustal assimilation below the
120 stability field of plagioclase rather than slab melting. Chiaradia et al. (2014) subsequently noted
121 that the variable, but on average elevated $\delta^{37}Cl$ (+0.55 to 2.66‰) of Rucu Pichincha samples is
122 consistent with the input in the volcano mantle source of few wt.% of different types of slab
123 fluids. As part of this debate, this study presents a new isotopic approach on minerals to better
124 assess the respective roles of source heterogeneity and crustal contamination in controlling the
125 composition of Pichincha magmas.
126

127 ## 3. Samples and methods

3.1 Samples

We picked 55 minerals from two dacite samples that correspond to two dome-forming eruptions of the Guagua Pichincha: PICH158 corresponds to a juvenile block from a block-and-ash flow deposit associated with the 1999-2001 eruption of the active Guagua Pichincha dome (the so-called Cristal dome); and PICH66D is a juvenile block from an explosive eruption of early Holocene age (9.8-10.9 ka BP) from the Toaza dome complex (Robin et al., 2010). We chose these two samples because they represent two dacites groups with different trace elements contents: Toaza dacites are enriched in some incompatible elements and display more variable trace elements ratios (Samaniego et al., 2010). The samples have 62-64 wt.% SiO_2, low concentrations of Heavy Rare Earth Elements (REE) (0.76-0.82 ppm Yb) and elevated Sr/Y ratios (59-63) (Appendix). PICH158 is porphyritic with phenocrysts of plagioclase (10–20 vol.%), amphibole (<10 vol.%), orthopyroxene (<5 vol.%), and Fe–Ti oxides (<1–2 vol.%) (Garcia-Aristizabal et al., 2007; Samaniego et al., 2010). Accessory phases include clinopyroxene and apatite. The dominantly glassy groundmass (~73-80 vol.%) is rhyolitic in composition and hosts microlites of the same mineral assemblage. PICH66D is a glassy pumice hosting phenocrysts of plagioclase (~5-10 vol.%), amphibole (~5 vol.%), orthopyroxene (<5 vol.%) and rare clinopyroxene and olivine.

Plagioclase shows euhedral habits and a wide compositional range (An_{29-77} for 1999-2001 dacite and An_{32-58} for the older Toaza dacite). It mostly shows reverse and oscillatory zoning patterns with frequent disequilibrium features such as dusty concentric zones and cores. Amphibole is the main mafic phase in the Guagua Pichincha dacites. We found two compositional groups: (1) common low-Al (6–10 wt.% Al_2O_3) magnesium– hornblende, and (2) scarce high-Al (10–15 wt.% Al_2O_3) tschermakite and magnesium–hastingsite. These different

amphibole compositions occur in the same sample, and in some cases high-Al cores are overgrown by low-Al rims. Orthopyroxene is also a common phenocryst with mostly euhedral habits and Mg# ranging from 62 to 85 (1999-2001 dacite) and 64 to 72 (Toaza dacite) and frequent normal zoning patterns. We should stress that orthopyroxene also occurs as overgrowth rims of anhedral olivine and clinopyroxene crystals. Fe-Ti oxides appear as microphenocrysts and microlites as well as inclusions in other minerals. Magnetite is the most common oxide although some ilmenites are also encountered. Lastly, clinopyroxene also appears as euhedral and subhedral phenocryts with a restricted compositional range (Mg# 71-83); and olivine appears as subhedral reactional crystals (Fo_{78-86}).

On the basis of a thermobarometric analysis, Samaniego et al. (2010) propose that the low-Al amphibole crystallizes at low pressure (100-250 MPa) that is well within the upper crust. In contrast, the crystallisation depth for high-Al amphiboles is less well constrained, but their compositions are similar to that of experimental amphiboles formed between 400 and 1000 MPa (Prouteau and Scaillet, 2003). Based on this observation, it is considered that the high-Al amphiboles crystallized at higher pressures and temperatures than the low-Al amphiboles (Samaniego et al., 2010).

Crystals of plagioclase, amphibole and orthopyroxene were chosen with sizes ranging from 0.6 to 1.5 mm on the longest axis. Nineteen amphibole, 4 orthopyroxene and 14 plagioclase phenocrysts from PICH158 and 14 amphibole and 4 plagioclase phenocrysts from PICH66D were analysed for major, trace and Pb isotope compositions.

3.2 Analytical methods

Minerals were picked under the binocular microscope in previously crushed and sieved samples. We focused on minerals with no (or almost no) attached glass to avoid leaching. Minerals were weighted on a Mettler micro-weighing scale with a precision of 0.001 mg, rinsed with H_2O MQ several times and dried in a clean hood. Minerals were transferred into savillex 7 mL vials. Minerals carrying small amount of rock matrix were leached with 3 mL of HCl 6N at 80°C for 3h. Then, dissolution was carried out with a solution of 0.5 mL of concentrated HF and 0.5 mL of concentrated HNO_3 at 90°C for about 48 h. A beaker containing 279 pg of ^{206}Pb-enriched NBS 983 spike was added to each series to determine Pb blank by isotopic dilution. After 24 h of attack, solutions were put in an ultrasound bath for 20 minutes and put back on the heating plate. Samples were then evaporated to dryness. One drop of concentrated HNO_3 was added and evaporated to dryness in order to remove Si-fluorides. Samples were fully dissolved in 500 µl of 7M HNO_3. An aliquot of 50 µl was taken to analyse major and trace elements while the remaining solution was used for Pb isotope analysis. Both solutions were evaporated to dryness.

Aliquots intended to major-trace element analysis were dissolved in 3 mL of 0.44N HNO_3 - 0.05N HF. Measurement of major and trace elements was carried out with an inductively coupled plasma quadrupole mass spectrometer (ICP-MS Agilent 7500). Concentrations were calibrated relative to 200 ppb (Na, Mg, Al, Ca, Fe) and 1-10 ppb (trace elements) synthetic solutions (Inorganic Ventures). Data and analytical errors are reported in Appendix. Leached minerals were also analysed, their concentrations are indicative. Major and trace element data on dissolutions are in good agreement with concentrations determined in-situ on thin sections (microprobe and LA-ICP-MS, unpublished data), comforting the idea that no xenocryst was picked.

195 Sample aliquots intended to Pb isotope analysis were dissolved in one drop of
196 concentrated HBr to complex Pb with Br as $PbBr_4^{2-}$ and $PbBr_3^-$, and evaporated to dryness. Lead
197 separation was carried out with 100-200 mesh AG1X8 anionic resin following the protocol of
198 Vlastélic et al. (2013). This procedure was slightly modified to avoid the evaporation step
199 between the two purification steps: the 1 mL solution used to elute Pb during the first chemistry
200 (solution B: 0.05 HNO_3 – 0.03N HBr) was transformed to solution used to load Pb during the
201 second chemistry (solution A: 0.05 HNO_3 – 0.2N HBr) by adding 20 µL of concentrated HBr.
202 Elutes were evaporated to dryness, dissolved in 2 drops of concentrated HNO_3 and evaporated to
203 dryness again. For all the protocol, concentrated HNO_3 and HBr acids used were distilled twice.
204 The amount of Pb separated ranges from 21 ng to 150 pg.
205 Lead isotopes were measured with a multi-collector inductively-coupled-plasma mass
206 spectrometer set up for high sensitivity (large interface pump, Jet sample cone and a X-skimmer
207 cone) (MC-ICP-MS Neptune *Plus*, Laboratoire Magmas et Volcans, Clermont-Ferrand, France).
208 The solutions were introduced in free-aspiration mode through an Aridus II desolvating nebulizer
209 system at a rate of 100 µl/min. The major ^{208}Pb, ^{207}Pb and ^{206}Pb isotopes were measured using
210 conventional $10^{11}\Omega$ resistors whereas ^{204}Pb was measured using a $10^{12}\Omega$ resistor. A Thallium
211 isotopic standard (NBS 997) was used to correct for mass fractionation. For a set of samples,
212 instability between Tl and Pb fractionation factors led us to correct for mass fractionation
213 externally by standard bracketing. These are marked up on Table 1. Two different modes of
214 analysis were used: a "regular" mode when the sample contained 1 ng of Pb or more, and a
215 "quick" mode otherwise. In the "regular" mode, samples were diluted in >1 ml of Tl NBS997 in
216 0.05N HNO_3 to obtain Pb concentrations in the range of 1-10 ppb and Pb/Tl ratios in the range 2-
217 5. The total Pb beam was 10 to $12x10^{-11}$ A for 5 ppb Pb solutions, and yielded 2 standard

deviations of 100 ppm or less after 50 measurement cycles. We found that the use of a $10^{12}\Omega$ instead of a $10^{11}\Omega$ resistor for measuring ^{204}Pb does not significantly improve the standard deviation of ^{204}Pb-normalized ratios for Pb concentration ≥1 ppb (^{204}Pb beam > $3x10^{-13}$ A). In "quick" mode, samples were diluted in a smaller volume (300 µL or 500 µL) to maintain the Pb concentration of the analysed solution above 0.5 ppb (^{204}Pb beam > $1.5x10^{-13}$ A), which allowed us to analyse precisely Pb amounts as low as 150 pg. For Pb concentration of 0.5 ppb, the use of the $10^{12}\Omega$ resistor maintains the in-run error below 500 ppm. Baseline and peak center were not performed at the beginning of the analysis, and isotopic ratios were measured from the onset of sample aspiration until sample exhaustion. The transient signal was treated offline as shown in Figure 2. Standard deviation estimated by repeated analysis of the NBS 981 standard in the same conditions as samples ("quick" mode) yielded 2 standard deviations between 284 and 569 ppm on ^{204}Pb-normalised isotopic ratios. Isotopic ratios corrected for mass fractionation were re-normalized to the NBS 981 value of Todt et al. (1996), to be easily compared with most of Pb isotope data from Ecuador (Ancellin et al., 2017). Blank contents are compiled in Table 1 along with their corresponding samples, and vary from 4.5 pg to 21.4 pg. During the course of this study, clean room Pb isotope composition was between 17.833 and 18.494 for $^{206}Pb/^{204}Pb$, 15.575 and 15.620 for $^{207}Pb/^{204}Pb$, 37.81 and 38.14 for $^{208}Pb/^{204}Pb$. Sample compositions were corrected for blank, although blank correction was smaller than the associated 2 standard deviation for each mineral analysed.

4. Results

4.1 Major and trace element composition of minerals

Major-trace element concentrations of minerals are reported in Appendix and rare earth element patterns are shown in Figure 3. Amphiboles show relatively flat rare earth element patterns, with slight enrichment of middle REE. They show a marked compositional evolution, from high-Al (up to 12.9 wt.% Al_2O_3), low incompatible element content (i.e. 1.6 ppm La), and no Eu anomaly [$Eu/Eu^*=Eu_N/(Sm_N \times Gd_N)^{0.5}=0.95$] to low-Al (as low as 5.8 wt.% Al_2O_3), high incompatible element content (i.e. 26 ppm La) and marked negative Eu anomaly (Eu/Eu*=0.41) (Fig. 4a, b). This evolution is also characterized by a factor of 3 to 5 increase of La/Yb, Nb/Zr and Nd/Pb, and a comparable decrease of Sr/Y, Ba/Nb, Be/La, Th/La and Rb/Th (e.g., Fig. 4c, d). Plagioclases display highly fractionated rare earth element patterns ($(La/Yb)_N \sim 10^2$) with strong positive Eu anomalies (5.4<Eu/Eu*<16.5). The four orthopyroxenes from PICH158 display slightly depleted to slightly enriched patterns with Eu negative anomalies (0.45<Eu/Eu*<0.69).

4.2 Pb isotope composition of minerals

Lead isotopic compositions of minerals are reported in Table 1. One amphibole appears as an outlier (A27 Pich158, *cf.* Table 1) and will be discussed separately. The $^{206}Pb/^{204}Pb$ (18.816-19.022) and $^{208}Pb/^{204}Pb$ (38.611-38.822) ratios of individual minerals display large and correlated variations, similar to those of lavas erupted during the 1 Ma Pichincha lifetime (Fig. 5a, b). The $^{207}Pb/^{204}Pb$ ratios display smaller variations (15.576-15.608) that do not correlate with $^{206}Pb/^{204}Pb$ or $^{208}Pb/^{204}Pb$ (Fig. 5c, d). Amphibole compositions are the most variable, with 10,411 ppm variation in $^{206}Pb/^{204}Pb$, compared to orthopyroxene (1,870 ppm) and plagioclase phenocrysts (1,063 ppm). Plagioclases generally define the radiogenic end-member composition, being more radiogenic that orthopyroxenes in PICH158 and more radiogenic than amphiboles in

PICH66D. Conversely the high-Al amphiboles define the unradiogenic end-member. The least radiogenic amphiboles and one orthopyroxene with $^{206}Pb/^{204}Pb < 18.95$ are less radiogenic than the Guagua Pichincha whole-rocks and do also plot above (higher $^{208}Pb/^{206}Pb$) the Rucu Pichincha whole-rock field (Fig. 5a, b). The Pb isotopic composition of minerals separated from PICH158 plot on both sides of the whole-rock composition, whereas all minerals separated from PICH66D are less radiogenic than whole rock. The $^{206}Pb/^{204}Pb$ ratios of amphiboles are between 8,336 ppm lower and 2,071 ppm higher than host rock for PICH158, and range between 1,981 and 8,601 ppm lower than host rock in PICH66D. Plagioclases are more radiogenic than host rock in PICH158 (up to 2,552 ppm higher $^{206}Pb/^{204}Pb$) but less radiogenic in PICH66D (up to 1,913 ppm lower $^{206}Pb/^{204}Pb$). Orthopyroxenes of PICH158 are less radiogenic than host rock, with 1,177 ppm lower $^{206}Pb/^{204}Pb$ on average. As shown on Figure 6, $^{206}Pb/^{204}Pb$ ratios of minerals show an overall increase during the crystallization sequence inferred from the extent of plagioclase fractionation (Eu/Eu*). This trend is accompanied by a marked decrease of $^{206}Pb/^{204}Pb$ variability, from ca. 6300 ppm in high-Al amphiboles to less than 1000 ppm in plagioclases.

5. Discussion

5.1. Minerals as records of a complex magmatic system

Most minerals analysed are in isotopic disequilibrium amongst themselves. It is clear from the scattering of Pb isotope data that minerals hosted within a hand-size rock sample are not genetically related through a closed system evolution of a single batch of parental melt. Instead, minerals are snapshots of magma evolution in the crust, recording silicate-melt isotope compositions at different times and places in the magmatic system of the Guagua Pichincha

286 volcano. Indeed, isotopic disequilibrium amongst minerals shows that most crystals present in a
287 magmatic rock are antecrysts that could be rimmed by equilibrium "phenocrystic" material
288 (Davidson et al., 2007). These observations agree with the concept of a transcrustal magmatic
289 system formed by a continuous crystal mush where eruptible melts gather crystals with distinct
290 pre-eruptive histories from different regions of the sub-volcanic system shortly before eruption
291 (Cashman et al., 2017). The time lapse between the two studied eruptions (<10 ka) is similar to
292 or shorter than the estimated differentiation time in crust (10^3-10^5 years; Annen et al. 2006),
293 explaining why no significant difference is seen between the magmatic evolution of the two
294 samples. Concerning the amphibole A27-Pich158 (1 analysis over 55) that does not follow the
295 magmatic differentiation scheme proposed here (Figure 6), we propose that this crystal record a
296 different, albeit minor, differentiation process that do not involve an increase in Pb isotope ratio
297 while fractionating plagioclase. In other words, this amphibole registered a differentiation
298 scheme where fractionation is associated with very minor crustal assimilation.
299 This diversity of signatures recorded in amphiboles, plagioclases and pyroxenes is very
300 likely to be registered as zonation in the single minerals. Indeed, in-situ Sr isotope studies
301 (Tepley et al., 1999; Davidson et al., 2001) showed that mineral zoning could involve
302 significantly diverse isotope signatures between overgrowths. For instance, we analysed two
303 splits of an amphibole (A12 Pich66D) that broke during handling. The two dissolutions named
304 A12-1 and A12-2 gave significantly different results for MgO (14.8 *vs.* 13.3 wt.%), some trace
305 elements (more than 10% variations for Li, Sc, Cr, Ni, Cu, Rb, Sr, La, Ce, Pb, Th, U) and Pb
306 isotopes ($^{206}Pb/^{204}Pb$= 19.001 *vs.* 18.914; $^{20}Pb/^{204}Pb$= 15.606 *vs.* 15.620 ; $^{208}Pb/^{204}Pb$= 38.806 *vs.*
307 38.736), showing the diversity of what appeared to be a single mineral at the binocular
308 microscope. Hence, dissolution averages mineral heterogeneities and consequently the magmatic

history of each mineral, but allows to span a largest range of phases, from primitive to late-forming ones. In-situ analyses wouldn't be possible on those minerals due to low Pb concentrations.

5.2. Pb budget of whole rocks

The Pb budget of rocks has been estimated by combining the modal compositions reported in section 3.1 and the Pb concentrations of minerals and whole-rocks. It was assumed that the compositional variations of the studied minerals represent those occurring within whole-rocks. In PICH158, 90 wt.% of Pb is in the groundmass, 8.3 wt.% in plagioclases, 1.4 wt.% in amphiboles and 0.4 wt.% in orthopyroxenes. In PICH66D, 96 wt.% of Pb is in the groundmass, 3.6 wt.% in plagioclases and 0.4 wt.% in amphiboles. In both samples, high-Al amphiboles account for less than 0.2 % of the Pb budget, which explains why their unradiogenic Pb compositions have a little influence on whole-rock compositions (Fig. 5). The Pb composition of the groundmass, inferred by mass balance (Table 1), is slightly less radiogenic than whole-rock for PICH158 (189 ppm lower $^{206}Pb/^{204}Pb$ and 128 ppm lower $^{208}Pb/^{204}Pb$) and barely more radiogenic than whole-rock for PICH66D (72 ppm higher $^{206}Pb/^{204}Pb$ and 57 ppm higher $^{208}Pb/^{204}Pb$). This difference reflects the fact that plagioclases are more radiogenic than whole-rock in PICH158 but less radiogenic that whole-rock in PICH66D where the groundmass should represent the missing radiogenic end-member (Fig. 5b, c). A major outcome of the Pb mass balance is that late equilibrated melts and late forming minerals carry >99 wt.% of the Pb budget of rocks, whereas Pb-poor high-Al amphiboles contribute insignificantly (<1 wt.%). An unsolved issue concerns the isotopic homogeneity of plagioclases and, in particular the absence of plagioclases with unradiogenic Pb signatures, which must have formed to produce the Eu

anomalies of most amphiboles (Fig. 6). These early-formed plagioclases could represent the core of the large plagioclase phenocrysts, whose Pb budget and isotopic compositions are probably dominated by the late stage of growth. If this hypothesis is correct, which is supported by the petrology of Guagua Pichincha dacites that shows that Ca-rich compositions are rare and restricted to some plagioclase cores, then the rims of plagioclases must have even higher $^{206}Pb/^{204}Pb$ than the bulk plagioclases.

5.3. Crustal assimilation within the stability field of plagioclase

Most magmas ascending through the thick crust of the Ecuador arc assimilate crustal materials. The resulting compositional modifications of mantle melts depend on the nature and the amount of assimilated crust, which varies geographically (*cf.* Bryant et al., 2006; Hidalgo et al., 2012; Ancellin et al., 2017). For instance, the $^{143}Nd/^{144}Nd$ and $^{207}Pb/^{204}Pb$ signature of lavas indicates that assimilation of old continental crust increases eastwards at the country scale, and southward along the frontal arc (Ancellin et al., 2017). Pichincha is in the northwest region where the basement is made of accreted fragments of oceanic plateaus and island arcs (Fig. 1). Consistently, the lack of systematic $^{207}Pb/^{204}Pb$ variations during the crystallisation sequence (Fig. 5c, d), and generally in Pichincha whole-rocks (Bourdon et al. 2003; Chiaradia et al., 2009), indicates that Pichincha magmas do not assimilate old continental rocks. Hidalgo et al. (2012) pointed out that the basement rocks have similar Sr-Nd isotopic signatures as mantle-derived magmas, which limits the visible imprint of crustal assimilation on Sr and Nd isotopes. Conversely, the Pb isotope evolution during crystallisation implies that Pichincha magmas assimilate oceanic rocks with more radiogenic $^{206}Pb/^{204}Pb$ and $^{208}Pb/^{204}Pb$ than the mantle-derived melts. Figure 6 shows that the $^{206}Pb/^{204}Pb$ ratios increase abruptly within the stability

355 field of high-Al amphibole, where plagioclase starts to crystallise (onset of Eu anomaly), and
356 more gently subsequently. Such an evolution is consistent with the Pb-depleted primitive melts
357 being more prone to contamination than differentiated melts. It also shows that the trend of
358 increasing $^{206}Pb/^{204}Pb$ with differentiation indices that Chiaradia et al. (2009) identified in whole-
359 rocks results from contamination within the upper, and not lower crust.

360 In the $^{208}Pb/^{204}Pb$ *vs.* $^{206}Pb/^{204}Pb$ isotopic space (Fig. 5, 7), high-Al amphiboles with
361 Eu/Eu*>0.8 plot on a well-defined array (r^2=0.93) with a gentle slope of 0.82(±0.11), whereas
362 other amphiboles, orthopyroxenes and plagioclases define an array (r^2=0.78) with a steeper slope
363 of 1.11 (±0.09). This indicates that the most primitive high-Al amphiboles and later formed
364 minerals do not share the same source of Pb. In the $^{207}Pb/^{204}Pb$ *vs.* $^{206}Pb/^{204}Pb$ space, the
365 regression lines through high-Al amphiboles with Eu/Eu*>0.8 and later formed minerals have
366 similar, close to zero slopes (-0.019±0.086 and 0.001±0.036, respectively). Although the
367 regression lines are poorly defined (r^2<0.2), the slopes are between -0.26 and 0.22 (high-Al
368 amphiboles, Eu/Eu*>0.8) and -0.07 and 0.07 (late forming minerals and other high-Al
369 amphiboles) at a 95% confidence level. This indicates that the crustal contaminant must have
370 more radiogenic $^{206}Pb/^{204}Pb$ and $^{208}Pb/^{204}Pb$ than high-Al amphiboles but nearly identical
371 $^{207}Pb/^{204}Pb$. Such composition is quite rare in Ecuador where basement rocks with
372 $^{206}Pb/^{204}Pb$>19.1 and $^{208}Pb/^{204}Pb$>38.83 generally have $^{207}Pb/^{204}Pb$>15.65 (Fig. 7). The most
373 likely contaminant is the 90 Ma old oceanic plateau accreted 65-68 Ma ago and known as the
374 Guaranda terrain. This geological unit shows a wide range of $^{206}Pb/^{204}Pb$ and $^{207}Pb/^{204}Pb$
375 variations (e.g., 18.29<$^{206}Pb/^{204}Pb$<19.71), and a radiogenic end-member with moderate
376 $^{207}Pb/^{204}Pb$ (≤15.61) that resembles the HIMU component of the Galapagos Islands (Mamberti et
377 al., 2003) (Fig. 7). This radiogenic end-member component is a suitable contaminant for

Pichincha primitive magma (represented by the high-Al amphiboles), but small addition of material with higher $^{208}Pb/^{206}Pb$, probably of continental origin, must occur at shallower depth to explain the slightly steeper slope of other minerals (amphiboles with Eu/Eu*<0.8, orthopyroxenes and plagioclases) in $^{208}Pb/^{204}Pb$ *vs.* $^{206}Pb/^{204}Pb$ space.

This scenario requires that Pichincha magmas preferentially assimilate the radiogenic end-member of the Guaranda unit. Mamberti et al. (2003) noted that the radiogenic end-member of the Guaranda unit consists essentially of ankaramites with $19.59<^{206}Pb/^{204}Pb<19.71$, whereas the unradiogenic end-member includes mostly picrites with $18.29<^{206}Pb/^{204}Pb<18.40$. It is suggested that the most fusible clinopyroxene-rich lithology might preferentially melt when Pichincha magmas interact with the rocks of the Guaranda unit. Mafic granulite xenoliths frequently occur in Pichincha volcanic rocks (Chiaradia et al., 2009) raising the possibility that magma contamination arises while xenoliths are superheated above the liquidus during ascent. Brearley and Scarfe (1986) who determined experimentally the dissolution rate of mantle minerals between 5 and 30 kbar, found that clinopyroxene dissolves faster than olivine at low pressure (5 kbar), where olivine is the liquidus phase, whereas olivine dissolves faster than clinopyroxene at higher pressure where clinopyroxene is the liquidus phase. They modelled the dissolution of ultramafic xenoliths in ascending alkali magmas, and estimated that, for an ascent time of 100 h, 25°C superheating, and grain size of 2 cm, 90% of the pyroxenite, against *ca.* 1% of the peridotite, is dissolved. Thus, if the Pichincha magmas disrupt and entrain rocks from the Guaranda unit, they will preferentially melt the more fusible ankaramitic lithology carrying radiogenic Pb, leaving behind a picritic residue with unradiogenic Pb. The restitic xenolith E05130a carrying unradiogenic Pb ($^{206}Pb/^{204}Pb=18.861$; $^{207}Pb/^{204}Pb=15.588$; $^{208}Pb/^{204}Pb=38.587$; Chiaradia et al., 2009) could be a remnant of such process. Assuming that

401 mantle-derived melts with $^{206}Pb/^{204}Pb$ between 18.816 and 18.879 (range of the two most
402 primitive amphiboles with Eu/Eu*≥0.94) assimilate crustal rocks with $^{206}Pb/^{204}Pb$ of 19.655
403 (average of the four radiogenic ankaramites) and identical Pb content, then between 18 and 24%
404 crustal assimilation is needed to explain the $^{206}Pb/^{204}Pb$ of 19.015 of late stage melts (average of
405 plagioclases). Taking samples separately, the extent of crustal assimilation needed to explain
406 PICH158 and PICH66D Pb whole-rock compositions from their respective parental melts
407 recorded in A12-Pich-158 and A7-Pich-66D amphiboles are 19 and 21%, respectively. These
408 values are higher that the estimate of 7–14% inferred from modelling whole-rock $\delta^{18}O$ (Hidalgo
409 et al., 2012) but similar to those inferred for Central Andean mafic lavas (Kay et al., 1994;
410 Aitcheson and Forrest, 1994)

411

412 **5.4. Composition of melts before plagioclase fractionation**

413 The two most primitive amphiboles with no significant Eu anomaly provide an insight
414 into the composition of Guagua Pichincha melts before plagioclase fractionation. In Pb-Pb
415 isotope space, their isotopic Pb signatures plot in the region near the convergence point of the
416 three main arrays defined by Ecuadorian volcanoes (Ancellin et al., 2017), i.e. at $^{206}Pb/^{204}Pb$ =
417 18.85-18.97; $^{207}Pb/^{204}Pb$ = 15.585-15.625; $^{208}Pb/^{204}Pb$ = 38.60-38.75. This composition could
418 reflect a mantle component common to Ecuadorian volcanoes, from which three main
419 contamination trends radiate (Chiaradia et al., 2009). However, the situation is probably not as
420 simple. For instance, the Pilavo volcano, located 100km north of Pichincha in the Western
421 Cordillera (*cf.* Fig. 1), defines the radiogenic end-member of the Pichincha array (with
422 $^{206}Pb/^{204}Pb$ up to 19.15), suggesting that its magmas are more contaminated than those of
423 Pichincha. Yet, Pilavo volcano produces less differentiated basaltic andesites with mantle-like Sr

and Nd isotopic ratios (Chiaradia et al., 2011). This suggests that different types of primitive melts feed the Pichincha and the Pilavo volcanoes, which probably also applies to other Ecuadorian volcanoes.

The two most primitive amphiboles also provide an insight into the heterogeneity of melts before plagioclase fractionation. These two minerals indeed have contrasted isotopic composition: the amphibole A12-Pich-158 has lower $^{206}Pb/^{204}Pb$ (18.816 *vs.* 18.879), and slightly lower $^{208}Pb/^{204}Pb$ (38.611 *vs.* 38.648) than A7-Pich-66D. It plots away from Pichincha whole rock field, whereas A7-Pich-66D plots very close (Fig. 5a). Although these two amphiboles have similar compositions for many elements (LREE, HREE, Ba, Zr, Nb, Zn, Cr, Co), some differences exist. For instance, A12-Pich158 is enriched in Cu, Li, Rb and Pb compared to A7-Pich66D (by factors of 23.3, 1.6, 1.8, 2.2 respectively) while being depleted in Al_2O_3 (9.76 *vs.* 12.4 wt.%) and Ti (0.42 *vs.* 1.23 wt.%).

Large variations of Li and Cu concentration have been reported in amphiboles from the 2004-2005 Mount St. Helens dacite (Rowe et al., 2008). These were ascribed to the partitioning of Li and Cu into a fluid phase that exsolves during magma ascent, so that the Li and Cu content of amphibole, as Al_2O_3, would record the depth of amphibole crystallization (Rowe et al., 2008). This explanation does not hold here because A12-Pich-158 has lower Al_2O_3 than A7-Pich-66D (Al_2O_3= 9.76 *vs.* 12.4 wt.% respectively) (Fig. 4a). Instead, the different chemical and isotopic compositions of the two primitive amphiboles of the Guagua Pichincha are better explained if A12-Pich-158 crystal grew in a melt enriched in fluid mobile elements (Li, Cu, Rb, Pb) that does not share the same source as the parental melt of A7-Pich-66D. These two types of melt unlikely result from assimilation or melting of lower crust but could correspond to stronger or lesser

446 metasomatism of the mantle wedge by slab melts and/or slab dehydration fluids, as previously
447 proposed by Samaniego et al., (2010).

448

449 **5.5. Long-term geochemical evolution of the Pichincha volcanic complex**

450 As many volcanoes in northern Ecuador, Pichincha volcanic complex experienced an
451 early calc-alkaline stage (Rucu volcano) before producing lavas with "adakitic" affinity (Guagua
452 volcano) (Samaniego et al., 2010). There is a debate on the origin of this transition, and in
453 particular on whether the so-called "adakitic" signature (high La/Yb and Sr/Y ratios, and low Yb
454 content) reflects the contribution of slab melts, or, alternatively, deep differentiation of melts
455 within the stability field of garnet (Chiaradia et al., 2009). We addressed this issue by comparing
456 the trace element signature of melts in equilibrium with the two most primitive amphiboles of the
457 Guagua Pichincha (A12-Pich-158 and A7-Pich-66D) to that of Rucu Pichincha primitive melts
458 recorded in olivine-hosted melt inclusions (Le Voyer et al., 2008). Even though these samples
459 are of different nature, they are the most primitive objects available of Rucu and Guagua
460 Pichincha. We found that melts in equilibrium with Guagua Pichincha high-Al amphiboles are
461 enriched in La and Y by factors of 2.5 and 1.5 respectively, and have on average 50% higher
462 La/Yb and Sr/Y ratios and 50% lower Ba/Nb ratio compared to the Rucu Pichincha primitive
463 melts (Fig. 8, partition coefficients from Tiepolo et al., 2007). This indicates that, if this
464 comparison stands, the Guagua Pichincha volcano is fed by melts that are enriched in
465 incompatible elements but depleted in fluid-mobile elements compared to the Rucu Pichincha
466 volcano, as suggested by whole-rock compositions (Samaniego et al., 2010). On the other hand,
467 the melts of the two volcanoes have identical Sm/Yb ratios (Fig. 8), indicating that they
468 underwent the same extent of garnet fractionation and evolved at similar depth. Assuming the

main source of fluid-mobile elements is the subduction component, we propose that a depletion of these elements in primitive melts through time reflects a change in subduction input into the mantle wedge. If magmas feeding the lower crust are depleted in fluid-mobile elements and enriched in incompatible elements, then, as fractionation goes in the deep crust, this difference in composition would get imprinted in the crust as well, reflecting a deeper change in magmas evolution.

6. Conclusions

The minerals hosted in hand-size dacite samples from the Guagua Pichincha volcano show large $^{206}Pb/^{204}Pb$ variations (>1%) that are comparable to the range of whole-rocks of the Pichincha Volcanic Complex. Amphiboles and orthopyroxenes record an increase of $^{206}Pb/^{204}Pb$ during the crystallization of plagioclase, which indicates that Guagua Pichincha magmas are contaminated within the upper crust. The most likely contaminant is the radiogenic ankaramites of the Guaranda unit, an accreted ocean plateau making the basement of the western Cordillera. The extent of crustal assimilation needed to explain the increase of $^{206}Pb/^{204}Pb$ from the two most primitive amphiboles to their respective host rocks is *ca.* 20%. Such a contamination is higher than previous estimates and contributes, together with melt mixing, to erase the heterogeneity of deep melts. The two most primitive amphiboles with no significant Eu anomaly also provide an insight into the heterogeneity of Guagua Pichincha melts before plagioclase crystallization. These melts have different $^{206}Pb/^{204}Pb$ ratios (18.816-18.879) and contents of fluid-mobile elements (Li, Cu, Rb, Pb) that are likely inherited from the heterogeneity of the metasomatic agent. Melts in equilibrium with the two most primitive amphiboles of the Guagua Pichincha are enriched in incompatible elements but depleted in fluid-mobile elements compared to the

olivine-hosted melt inclusions of the older Rucu Pichincha. This supports previous conclusions based on whole-rock compositions that the mantle source of the Pichincha Volcanic Complex has changed through time (Samaniego et al., 2010). Precise measurements of single grain Pb isotope compositions by wet chemistry proved useful to identify crustal processes and the heterogeneity of mantle-derived melts in a complex volcanic setting.

APPENDIX

A supplementary table with major and trace element as well as Pb isotope compositions of whole-rock and mineral samples is provided.

ACKNOWLEDGMENTS

We thank Chantal Bosq and Jean-Luc Piro for analytical support, Estelle Rose-Koga for constructive discussions and Emilie Bruand for her advice on an early version of the manuscript. We also thank Catherine Chauvel for handling the edition of this study, Suzanne Kay and an anonymous reviewer for their comments which helped improving the manuscript. This work was supported by the French Government Laboratory of Excellence initiative ANR-10-LABX-0006, the Région Auvergne and the European Regional Development Funds. It is part of an Ecuadorian-French cooperation program (Laboratoire Mixte International "Séismes et Volcans dans les Andes du Nord") carried out between the Instituto Geofísico, Escuela Politécnica Nacional (IG-EPN), and the Institut de Recherche pour le Développement (IRD). This is Laboratory of Excellence ClerVolc contribution number XXX.

513 **Figure captions**

514

515 Figure 1: (a) Geodynamical setting of the Ecuadorian arc. Dashed yellow line highlights
516 Ecuadorian border. Quaternary volcanic edifices are displayed as black-circled white shapes. (b)
517 Simplified geological map of Ecuador showing the main oceanic and continental units,
518 quaternary volcanic edifices and the location of the Pichincha Volcanic Complex. Oceanic units
519 making the basement of the Western Cordillera are drawn after Jaillard et al. (2008), namely
520 Macuchi terrain, Guaranda terrain and San Juan terrain.

521

522 Figure 2: Example of transient signal obtained during "quick mode" acquisition of Pb isotopes
523 on the Neptune Plus MC-ICP-MS. Here is the measurement of sample A4 from PICH 66D that
524 contained 354 pg of Pb dissolved in 300 µL of 0.05N HNO3–1ppb NBS997 Tl. The signal
525 plateau includes 15 cycles that were selected to calculate the isotope composition.

526

527 Figure 3: Spider diagram displaying the trace element compositions of dissolved amphibole,
528 plagioclase and pyroxene crystals of PICH 158 and PICH66D, as well as the two whole-rocks
529 PICH 158 and PICH 66D. Trace elements are normalized to chondrites (Sun and McDonough,
530 1989). For sake of clarity, only minerals that stands at the extreme compositions are labelled.

531

532 Figure 4: Amphibole composition versus amphibole Eu anomaly. The Eu anomaly is defined as
533 follows: $Eu/Eu^{*}=Eu_N/(Sm_N \times Gd_N)^{0.5}$, where N refers to concentration normalized to the
534 primitive mantle. (a) Al_2O_3 content (wt. %). The boundary between low- and high-Al amphiboles
535 is between 9.6 and 10.9 wt.% Al_2O_3 (Garcia-Aristizabal et al., 2007; Samaniego et al. 2010). (b)

La content (ppm). (c) Ba/Nb ratio. (d) Nd/Pb ratio. Amphiboles with Eu/Eu* >0.7 are red-rimmed. In the manuscript, Eu anomaly is used as an indicator of plagioclase fractionation and, as a result, of differentiation. This is consistent with the correlation between La content, Ba/Nb, Nd/Pb and Eu/Eu* of amphiboles. We assume that changing parental magma composition have a stronger effect on amphibole geochemistry than variations in partition coefficients linked to crystallising amphiboles from a more or less evolved magma. We selected elemental pairs (Ba/Nb and Nd/Pb) for which partition coefficients in amphibole would respond similarly to changes in temperature and matrix (Nandedkar et al., 2016). Then, variations of those ratios in amphibole would denote a change in parental magma compositions. Nevertheless, it is possible that secondary effects play a role in changing Eu/Eu*. Oxygen fugacity influences the Eu^{3+}/Eu^{2+} ratio (Burnham et al., 2015) and thus the size of Eu anomalies in magmas and related plagioclases. However, change in fO_2 should be small in our magmatic column. For instance, Gaillard et al. (2015) showed that between 10kbar and surface, logfO2 increases from 1.3 to 1.6 (relative to QFM buffer) in oxidized arc magmas. Within this small range of oxygen fugacity, there is almost no change in Eu^{3+}/Eu^{2+} with magma composition (Burhnam et al., 2015).

Figure 5: $^{208}Pb/^{204}Pb$ *vs.* $^{206}Pb/^{204}Pb$ plot showing the composition of individual minerals. The composition of PICH158 and PICH66D host-rocks, and the fields of Guagua and Rucu Pichincha whole-rocks are shown for comparison (after Bourdon et al., 2003; Bryant et al., 2006; Chiaradia et al., 2009; Ancellin et al., 2017). Error bars (± 2σ) are displayed when larger than symbol size. High-Al amphiboles after figure 4.

Figure 6: Mineral $^{206}Pb/^{204}Pb$ versus mineral Eu anomaly. Plagioclases with large positive Eu anomalies are shown on a separate scale. Symbols are as in Figure 4. Error bars (± 2σ) are displayed when larger than symbol size. The boundary between high-Al and low-Al amphiboles at Eu/Eu*=0.7 is inferred from Figure 4. Symbols as figure 5.

Figure 7: $^{208}Pb/^{204}Pb$ *vs.* $^{206}Pb/^{204}Pb$ (a) and $^{207}Pb/^{204}Pb$ *vs.* $^{206}Pb/^{204}Pb$ (b) diagrams. Regression lines through Guagua and Rucu Pichincha whole rocks (plain line), high-Al amphiboles with Eu/Eu*>0.8 (loose dashed line) and other amphiboles, orthopyroxenes and plagioclases (tight dashed line) are shown. Correlation coefficients and standard errors on slopes and intercepts are indicated. Compositional fields are shown for continental (C) basement rocks (Chaucha - Loja - Tahuin - Alao terranes (Chiaradia et al., 2004) and granulites and amphibolites of the Western Cordillera (Amortegui, 2007)), accreted ocean island arc of Macuchi (M) (Chiaradia and Fontbote, 2001), Guaranda (G) and San Juan (SJ) accreted oceanic plateaus (Mamberti et al., 2003, 2004). Symbols as figure 5.

Figure 8: Comparison between Guagua Pichincha and Rucu Pichincha primitive melts signatures. Guagua Pichincha primitive melts are assumed to be in equilibrium with the most primitive amphiboles A12-Pich-158 and A7-Pich-66D. Their compositions are calculated using the amphibole/melt partition coefficients of Tiepolo et al. (2007) (D_{La}=0.2, D_{Nb}=D_{Ba}=D_{Sr}=0.3; D_{Sm}=1, D_{Yb}=0.9, D_{Y}=1.1). Rucu Pichincha primitive melts are those of olivine-hosted melt inclusions (Le Voyer et al., 2008). All compositions are normalized to the average composition of Rucu Pichincha primitive melts.

References

Aitcheson, S. J., Forrest, A. H., 1994. Quantification of crustal contamination in open magmatic systems. Journal of Petrology 35, 461-488. doi:10.1093/petrology/35.2.461

Amortegui, A., 2007. Nature et évolution métamorphiques des terrains océaniques en Equateur: Conséquences possibles sur la genèse des magmas adakitiques. Unpublished PhD Thesis, University Joseph Fourier, Grenoble, France, 179 p.

Ancellin, M.-A., Samaniego, P., Vlastélic, I., Nauret, F., Gannoun, A., Hidalgo, S., 2017. Across-arc versus along-arc Sr-Nd-Pb isotope variations in the Ecuadorian volcanic arc: Geochem. Geophys. Geosyst. 18, doi:10.1002/2016gc006679.

Annen, C., Blundy, J.D., and Sparks, R.S.J., 2006. The genesis of intermediate and silicic magmas in deep crustal hot zones: Journal of Petrology 47, 505–539, doi:10.1093/petrology/egi084.

Bourdon, E, Eissen, J.P., Gutscher, M.A., Monzier M., Hall M.L., Cotten J., 2003. Magmatic response to early aseismic ridge subduction: the Ecuadorian margin case (South America). Earth Planet. Sci. Lett. 205, 123–138. doi:10.1016/S0012-821X(02)01024-5

Burhnam A. D., Berry A. J., Halse H. R., Schofield P. F., Cibin G., Mosselmans J. F. W., 2015. The oxidation state of europium in silicate melts as a function of oxygen fugacity, composition and temperature. Chem. Geol. 411, 248-259. doi:10.1016/j.chemgeo.2015.07.002

Brearley, M., Scarfe, C.M., 1986. Dissolution rates of upper mantle minerals in an alkali basalt melt at high pressure: An experimental study and implications for ultramafic xenolith survival. J. Petrol. 27, 1157-1182. doi:10.1093/petrology/27.5.1157

603 Bryant, J.A., Yogodzinski, G.M., Hall, M.L., Lewicki, J.L., Bailey, D.G., 2006. Geochemical
604 constraints on the origin of volcanic rocks from the Andean Northern volcanic zone,
605 Ecuador: J. Petrol. 47, 1147–1175, doi:10.1093/petrology/egl006.
606 Cashman K. V., Sparks R. S. J., Blundy J. D., 2017. Vertically extensive and unstable magmatic
607 systems: a unified view of igneous processes. Science 355, eaag3055.
608 doi:10.1126/science.aag3055
609 Chiaradia, M., Fontboté, L., 2001. Radiogenic lead signatures in Au-rich VHMS ores and
610 associated volcanic rocks of the Early Tertiary Macuchi island arc (Western Cordillera of
611 Ecuador). Econ. Geol. 96, 1361–1378. doi:10.2113/gsecongeo.96.6.1361
612 Chiaradia, M., Fontboté, L., Paladines, A., 2004. Metal sources in mineral deposits and crustal
613 rocks of Ecuador (1°N–4°S): a lead isotope synthesis. Econ. Geol. 99, 1085–1106.
614 doi:10.2113/gsecongeo.99.6.1085
615 Chiaradia, M., Müntener, O., Beate, B., Fontignie, D., 2009. Adakite-like volcanism of Ecuador:
616 Lower crust magmatic evolution and recycling: Contrib. Mineral. Petrol. 158, 563–588,
617 doi:10.1007/s00410-009-0397-2.
618 Chiaradia, M., Müntener, O., Beate, B., 2011. Enriched basaltic andesites from mid-crustal
619 fractional crystallization, recharge and assimilation (Pilavo Volcano, Western Cordillera of
620 Ecuador). J. Petrol. 6, 1107-1141. doi:10.1093/petrology/egr020
621 Chiaradia, M., Barnes, J.D., Cadet-Voisin, S., 2014. Chlorine stable isotope variations across the
622 Quaternary volcanic arc of Ecuador. Earth Planet. Sci. Lett. 396, 22–33.
623 doi:10.1016/j.epsl.2014.03.062

624 Davidson J., Tepley III F., Palacz Z., Meffan-Main S., 2001. Magma recharge, contamination
625 and residence times revealed by in situ laser ablation isotopic analysis of feldspar in volcanic
626 rocks. Earth Planet. Sci. Lett. 184, 427-442. doi:10.1016/S0012-821X(00)00333-2
627 Davidson J. P., Morgan D. J., Charlier B. L. A., Harlou R., Hora J. M., 2007. Microsampling and
628 isotopic analysis of igneous rocks: implications for the study of magmatic systems. Annu.
629 Rev. Earth Planet. Sci. 35, 273-311. doi:10.1146/annurev.earth.35.031306.140211
630 Dungan, M.A., Davidson, J., 2004. Partial assimilative recycling of the mafic plutonic roots of
631 arc volcanoes: An example from the Chilean Andes. Geology 32, 773–776,
632 doi:10.1130/G20735.1.
633 Elliott, T., Plank, T., Zindler, A., White, W.M., Bourdon, B., 1997. Element transport from slab
634 to volcanic front at the Mariana Arc. J. Geophys. Res. 102, 14,991-15,019. doi:
635 10.1029/97JB00788
636 Farner, M.J., Lee, C.A., 2017. Effects of crustal thickness on magmatic differentiation in
637 subduction zone volcanism: A global study. Earth Planet. Sci. Lett. 470, 96–107,
638 doi:10.1016/j.epsl.2017.04.025.
639 Feininger, T., Seguin, M.K., 1983. Simple Bouguer gravity anomaly field and the inferred crustal
640 structure of continental Ecuador. Geology 11, 40–44. doi:10.1130/0091-
641 7613(1983)11<40:SBGAFA>2.0.CO;2
642 Garcia-Aristizabal, A., Kumagai, H., Samaniego, P., Mothes, P., Yepes, H., Monzier, M., 2007.
643 Seismic, petrologic, and geodetic analyses of the 1999 dome-forming eruption of Guagua
644 Pichincha volcano, Ecuador. J. Volcanol. Geotherm. Res. 161, 333–351,
645 doi:10.1016/j.jvolgeores.2006.12.007.

646 Gill, J.B., 1981. Orogenic Andesites and Plate Tectonics (P. J. Wyllie, Ed.): Berlin Heidelberg
647 New York, Springer-Verlag, doi:10.1007/978-3-642-68012-0.
648 Guillier, B., Chatelain, J.-L., Jaillard, E., Yepes, H., Poupinet, G., Fels, J.-F., 2001.
649 Seismological evidence on the geometry of the orogenic system in central-northern Ecuador
650 (South America). Geophys. Res. Lett. 28, 3749–3752. doi:10.1029/2001GL013257
651 Hawkesworth, C.J., Gallagher, K., Hergt, J.M., Mcdermott, F., 1993. Mantle and slab
652 contributions in arc magmas. Annual Review of Earth and Planetary Sciences 21, 175–204.
653 doi:10.1146/annurev.ea.21.050193.001135
654 Hidalgo, S., Gerbe, M. C., Martin, H., Samaniego, P., Bourdon, E., 2012. Role of crustal and
655 slab components in the Northern Volcanic Zone of the Andes (Ecuador) constrained by Sr–
656 Nd–O isotopes. Lithos 132–133, 180–192, doi:10.1016/j.lithos.2011.11.019.
657 Hildreth, W., Moorbath, S., 1988. Crustal contribution to arc magmatism in the Andes of Central
658 Chile. Contrib. Mineral. Petrol. 98, 455–489. doi:10.1007/BF00372365
659 Jaillard, E., Ordonez, M., Suarez, J., Toro, J., Iza, D, Lugo, W., 2004. Stratigraphy of the late
660 Cretaceous–Paleogene deposits of the Cordillera Occidental of central Ecuador: geodynamic
661 implications. J. South Am. Earth Sci. 17, 49–58. doi:10.1016/j.jsames.2004.05.003
662 Jaillard, E., Bengtson, P., Ordonez, M., Vaca, W., Dhondt, A., Suarez, J., Toro, J., 2008.
663 Sedimentary record of terminal Cretaceous accretions in Ecuador: The Yunguilla Group in
664 the Cuenca area, J. South Am. Earth Sci., 25, 133–144, doi:10.1016/j.jsames.2007.08.002.
665 Jagoutz, O., Schmidt, M.W., 2012. The formation and bulk composition of modern juvenile
666 continental crust: The Kohistan arc. Chem. Geol. 298–299, 79–96,
667 doi:10.1016/j.chemgeo.2011.10.022.

668 Kay S.M., Coira B., Viramonte J., 1994. Young mafic back arc volcanic rocks as indicators of
669 continental lithospheric delamination beneath the Argentine Puna plateau, central Andes. J.
670 Geophys. Res. 99, 24,323-24,339, doi:10.1029/94JB00896
671 Kelemen, P.B., Hanghoj, K., Greene, A.R., 2007. One view of the geochemistry of subduction-
672 related magmatic arcs, with an emphasis on primitive andesite and lower crust. Treatise on
673 Geochemistry, Second Edition 4, 749–806, doi:10.1016/B978-0-08-095975-7.00323-5.
674 Le Voyer, M., Rose-Koga, E.F., Laubier, M., Schiano, P., 2008. Petrogenesis of arc lavas from
675 the Rucu Pichincha and Pan de Azucar volcanoes (Ecuadorian arc): Major, trace element,
676 and boron isotope evidences from olivine-hosted melt inclusions. Geochem. Geophys.
677 Geosyst. 9, Q12027, doi:10.1029/2008GC002173.
678 Leeman, W.P., 1983. The influence of crustal structure on compositions of subduction-related
679 magmas. J. Volcanol. Geotherm. Res. 18, 561–588, doi:10.1016/0377-0273(83)90026-4.
680 Mamberti, M., Lapierre, H., Bosch, D., Jaillard, E., Ethien, R., Hernandez, J., Polve M., 2003.
681 Accreted fragments of the Late Cretaceous Caribbean–Colombian Plateau in Ecuador.
682 Lithos 66, 173– 199. doi:10.1016/S0024-4937(02)00218-9
683 Mamberti, M., Lapierre, H., Bosch, D., Jaillard, E., Hernandez, J., Polve M., 2004. The early
684 cretaceous San Juan plutonic suite, Ecuador: a magma chamber in an oceanic plateau. Can.
685 J. Earth Sci. 41, 1237-1258.
686 Mantle, G.W., Collins, W.J., 2008. Quantifying crustal thickness variations in evolving orogens:
687 Correlation between arc basalt composition and Moho depth. Geology 36, 87–90,
688 doi:10.1130/G24095A.1.

McCulloch, M.T., Gamble, J.A., 1991. Geochemical and geodynamical constraints on subduction zone magmatism. Earth Planet. Sci. Lett. 102, 358–374. doi:10.1016/0012-821X(91)90029-H

Monzier, M., Robin, C., Samaniego, P., Hall, M.L., Cotten, J., Mothes, P., Arnaud, N., 1999. Sangay volcano, Ecuador: structural development, present activity and petrology. J. Volcanol. Geotherm. Res. 90, doi:10.1016/S0377-0273(99)00021-9.

Nandedkar R. H., Hürlimann N., Ulmer P., Müntener O., 2016. Amphibole-melt trace element partitioning of fractionating calc-alkaline magmas in the lower crust: an experimental study. Contrib. Mineral. Petrol. 171:71. doi:10.1007/s00410-016-1278-0

Narváez, D., Rose-Koga, E., Samaniego, P., Koga, K.T., Hidalgo, S., 2016. Constraining magma sources using primitive olivine-hosted melt inclusions from Puñalica and Sangay volcanoes (Ecuador). Contrib. Mineral. Petrol. 173, 80. doi:10.1007/s00410-018-1508-8.

Nauret, F., Samaniego, P., Ancellin, M.-A., Tournigand, P.-Y. Le Pennec, J.-L., Vlastelic, I., Gannoun, A., Hidalgo, S., Schiano, P., 2018. The genetic relationship between andesites and dacites at Tungurahua volcano, Ecuador. J. Volcanol. Geotherm. Res. 349, 283-297. doi:10.1016/j.jvolgeores.2017.11.012

Nocquet, J.-M., Villegas-Lanza, J. C., Chlieh, M., Mothes, P. A., Rolandone, F., Jarrin, P., (…), Yepes, H., 2014. Motion of continental slivers and creeping subduction in the northern Andes. Nature Geosciences 7, 287-291. doi:10.1038/NGEO2099

Paul, B., Woodhead, J.D., Hergt, J., Danyushevsky, L., Kunihiro, T., Nakamura, E., 2011. Melt inclusion Pb-isotope analysis by LA-MC-ICPMS: Assessment of analytical performance and application to OIB genesis. Chem. Geol. 289, 210–223. doi:10.1016/j.chemgeo.2011.08.005.

711 Prouteau, G., Scaillet, B., 2003. Experimental constraints on the origin of the 1991 Pinatubo
712 dacite. J. Petrol. 44, 2203–2241. doi:10.1093/petrology/egg075
713 Reinhard, A.A., Jackson, M.G., Koornneef, J.M., Rose-Koga, E.F., Blusztajn, J., Konter, J.G.,
714 Koga, K.T., Wallace, P.J., Harvey, J., 2018. Sr and Nd isotopic compositions of individual
715 olivine-hosted melt inclusions from Hawai'i and Samoa: Implications for the origin of
716 isotopic heterogeneity in melt inclusions from OIB lavas. Chem. Geol. 495, 36–49.
717 doi:10.1016/j.chemgeo.2018.07.034
718 Ribeiro, J. M., Maury, R. C., Grégoire, M., 2016. Are adakites slab melts or high-pressure
719 fractionated mantle metls? J. Petrol. 57, 839-862. doi: 10.1093/petrology/egw023
720 Robin, C., Samaniego, P., Le Pennec, J.L., Fornari, M., Mothes, P., van der Plicht, J., 2010. New
721 radiometric and petrological constraints on the evolution of the Pichincha volcanic complex
722 (Ecuador). Bull. Volcanol. 72, 1109–1129. doi:10.1007/s00445-010-0389-0.
723 Rose-Koga, E.F., Koga, K.T., Schiano, P., Le Voyer, M., Shimizu, N., Whitehouse, M.J.,
724 Clocchiatti, R., 2012. Mantle source heterogeneity for South Tyrrhenian magmas revealed
725 by Pb isotopes and halogen contents of olivine-hosted melt inclusions. Chem. Geol. 334,
726 266–279. doi:10.1016/j.chemgeo.2012.10.033.
727 Rowe, M.C., Kent, A.J.R., Thornber, C.R., 2008. Using amphibole phenocrysts to track vapor
728 transfer during magma crystallization and transport: an example from Mount St. Helens,
729 Washington. J. Volcanol. Geotherm. Res. 178, 593–607.
730 doi:10.1016/j.jvolgeores.2008.01.012
731 Samaniego, P., Robin, C., Chazot, G., Bourdon, E., Cotten, J., 2010. Evolving metasomatic agent
732 in the Northern Andean subduction zone, deduced from magma composition of the long-

733 lived Pichincha volcanic complex (Ecuador). Contrib. Mineral. Petrol. 160, 239–260,
734 doi:10.1007/s00410-009-0475-5.
735 Schiano, P., 2003. Primitive mantle magmas recorded as silicate melt inclusions in igneous
736 minerals. Earth Sci. Rev. 63, 121–144, doi:10.1016/S0012-8252(03)00034-5.
737 Schmidt, M.W., Jagoutz, O., 2017. The global systematics of primitive arc melts. Geochem.
738 Geophys. Geosyst. 18, 2817-2854, doi:10.1002/2016GC006699.
739 Sobolev, A.V., 1996. Melt inclusions in minerals as a source of principle petrological
740 information: Petrology 4, 209–220.
741 Sun, S. S. and McDonough, W. F., 1989. Chemical and isotopic systematics of oceanic basalts:
742 implications for mantle composition and processes. Geological Society of London, Spec.
743 Pub. 42, 313-345. doi: 10.1144/GSL.SP.1989.042.01.19
744 Taylor, H.P., 1980. The effects of assimilation of country rocks by magmas on $^{18}O/^{16}O$ and
745 $^{87}Sr/^{86}Sr$ systematics in igneous rocks. Earth Planet. Sci. Lett. 47, 243–254,
746 doi:10.1016/0012-821X(80)90040-0.
747 Tepley III F., Davidson J. P., Clynne M. A., 1999. Magmatic interactions as recorded in
748 plagioclase phenocrysts of Chaos Crags, Lassen Volcanic Center, California. Journal of
749 Petrology 40, 787-806. doi:10.1093/petroj/40.5.787
750 Tiepolo, M., Oberti, R., Zanetti, A., Vannucci, R., Foley, S.F., 2007. Trace-element partitioning
751 between amphibole and silicate melt. Rev. Mineral. Geochem. 67, 417–452,
752 doi:10.2138/rmg.2007.67.11.
753 Todt, W., Cliff, R.A., Hanser, A., Hofmann, A.W., 1996. Evaluation of a $^{202}Pb–^{205}Pb$ double
754 spike for high-precision lead isotope analysis, in Earth Processes. In Reading the Isotopic
755 Code (eds. A. Basu and S. Hart). AGU, pp. 429–437.

Trenkamp, R., Kellogg, J.N., Freymueller, J.T., Mora, H.P., 2002. Wide plate margin deformation, southern Central America and northwestern South America, CASA GPS observations. J. South Am. Earth Sci. 15, 157-171. doi:10.1016/S0895-9811(02)00018-4

Turner, S.J., Langmuir, C.H., Katz, R.F., Dungan, M.A., Escrig, S., 2016. Parental arc magma compositions dominantly controlled by mantle-wedge thermal structure. Nat. Geosci. 9, 772–776, doi:10.1038/NGEO2788.

Vaca, S., Vallée, M., Nocquet, J.-M., Alvarado, A., 2019. Active deformation in Ecuador enlightened by a new waveform-based catalog of earthquake focal mechanisms. J. South Am. Earth Sci. 93, 449-461. doi:10.1016/j.jsames.2019.05.017

Vlastelic, I., Staudacher, T., Deniel, C., Devidal, J. L., Devouard, B., Finizola, A., Télouk, P., 2013. Lead isotopes behavior in the fumarolic environment of the Piton de la Fournaise volcano (Reunion Island). Geochim. Cosmochim. Acta, 100, 297–314. doi:10.1016/j.gca.2012.09.016

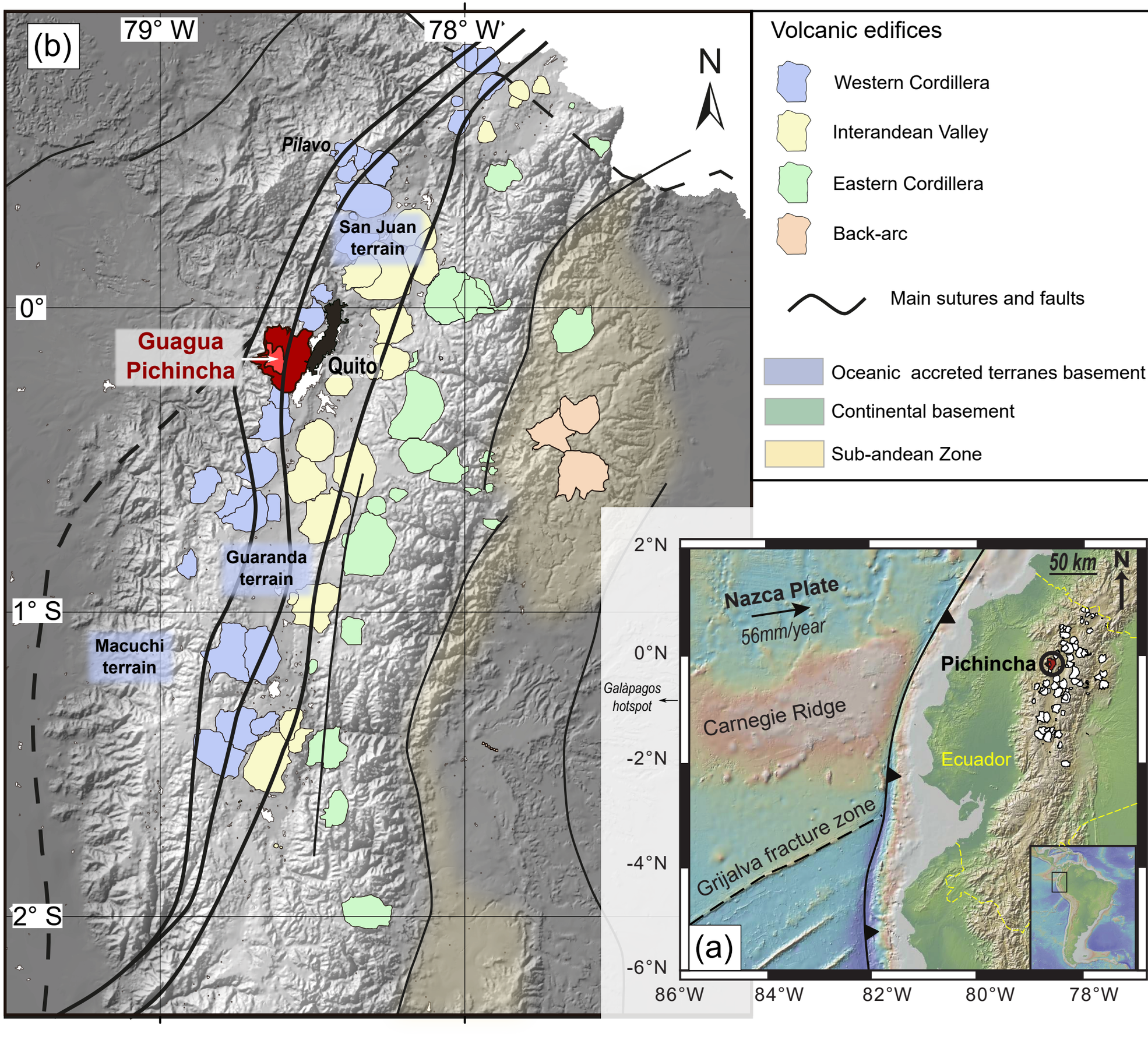
(b)
79° W
78° W
N
Pilavo
San Juan terrain
0°
Guagua Pichincha
Quito
Guaranda terrain
1° S
Macuchi terrain
2° S
Volcanic edifices
Western Cordillera
Interandean Valley
Eastern Cordillera
Back-arc
Main sutures and faults
Oceanic accreted terranes basement
Continental basement
Sub-andean Zone
2°N
0°N
-2°N
-4°N
-6°N
86°W
84°W
82°W
80°W
78°W
Galàpagos hotspot
Nazca Plate
56mm/year
Carnegie Ridge
Grijalva fracture zone
Pichincha
Ecuador
50 km
N
(a)

Fig.2

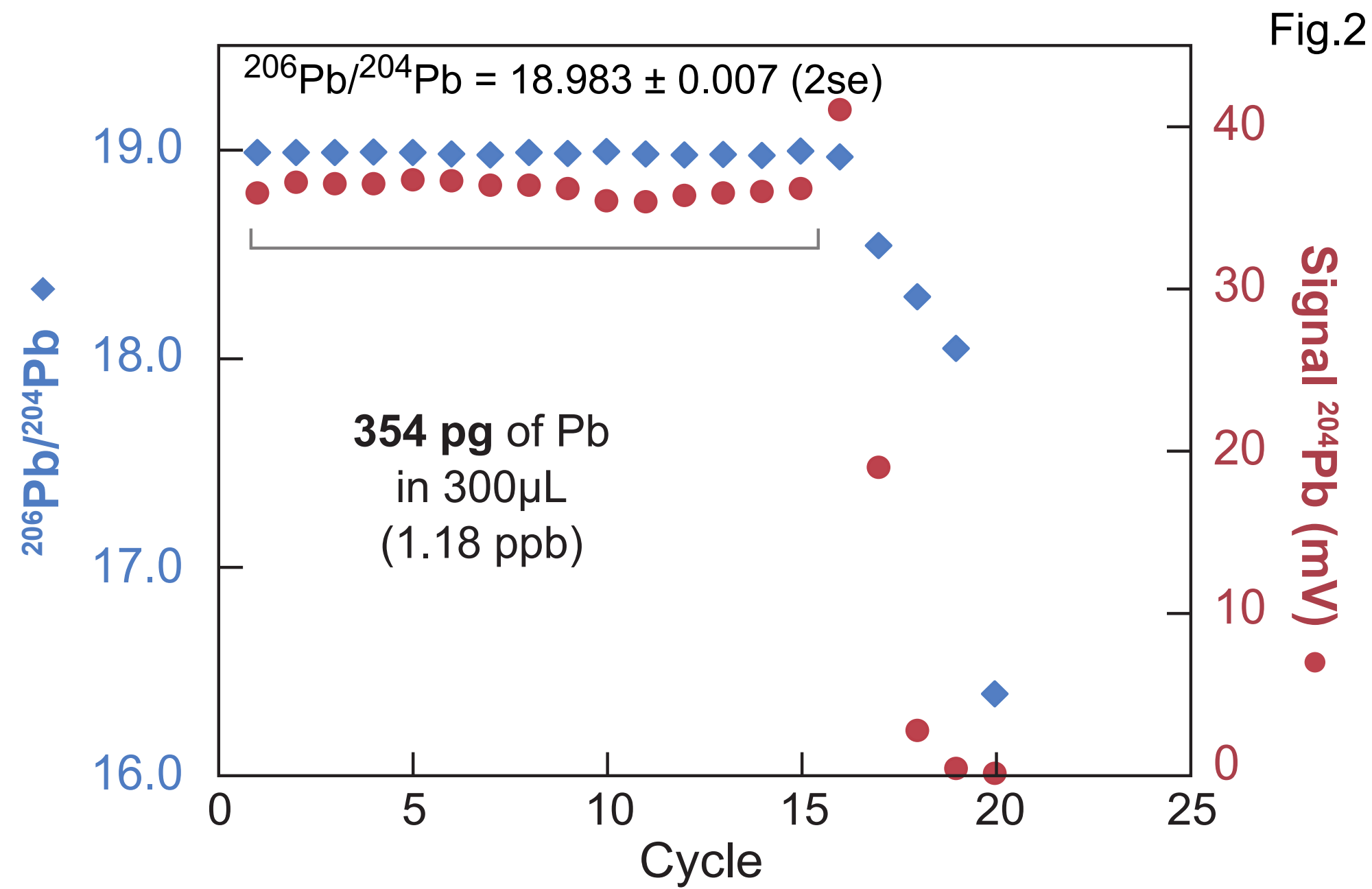
$^{206}Pb/^{204}Pb$ = 18.983 ± 0.007 (2se)
354 pg of Pb
in 300μL
(1.18 ppb)
$^{206}Pb/^{204}Pb$
^{204}Pb (mV)
Cycle
19.0
18.0
17.0
16.0
40
30
20
10
0
0
5
10
15
20
25

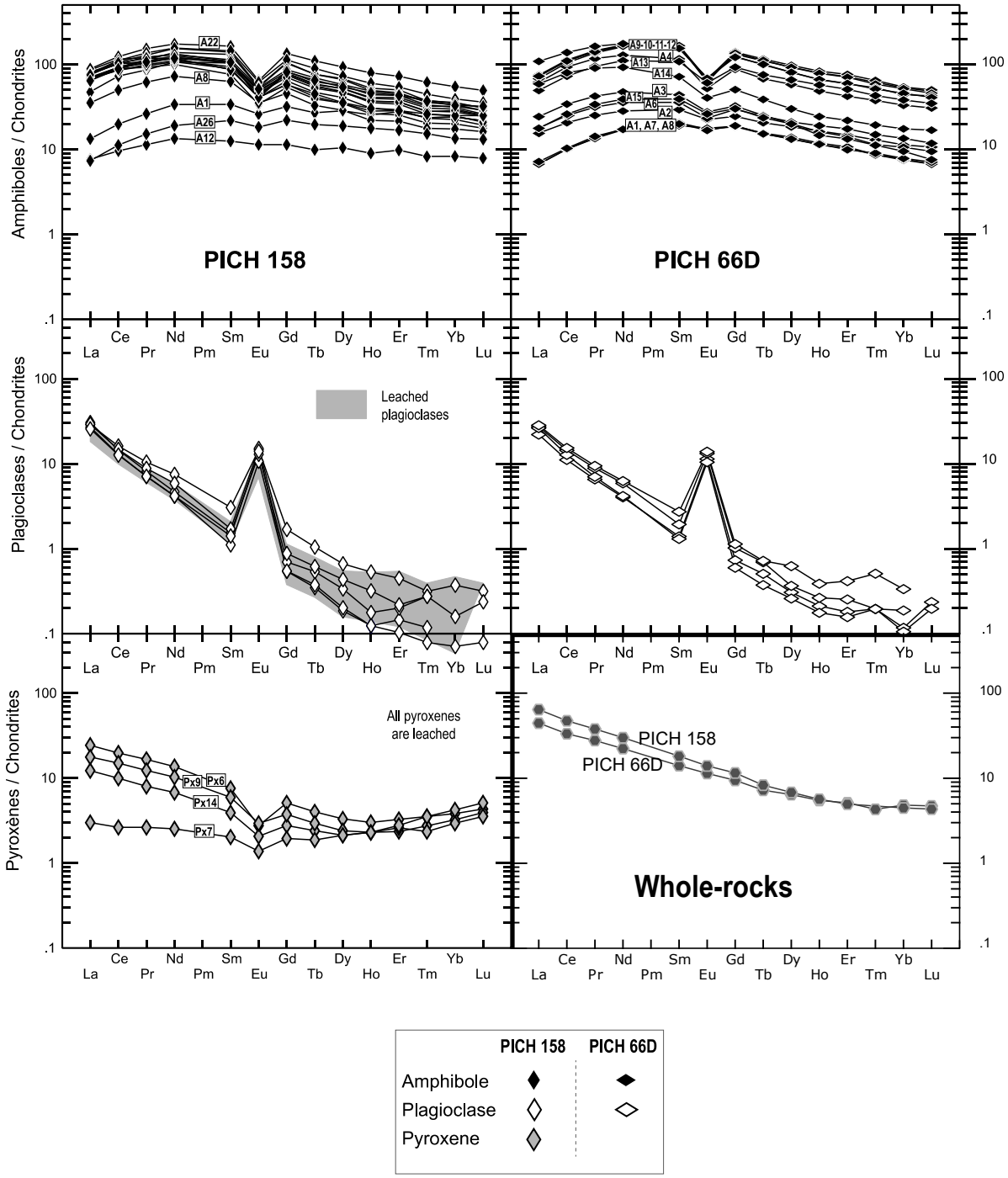
Amphiboles / Chondrites
Plagioclases / Chondrites
Pyroxènes / Chondrites
PICH 158
PICH 66D
A22
A8
A1
A26
A12
A9-10-11-12
A13
A4
A14
A15
A3
A6
A2
A1, A7, A8
Leached plagioclases
All pyroxenes are leached
Px9
Px6
Px14
Px7
PICH 158
PICH 66D
Whole-rocks
La Ce Pr Nd Pm Sm Eu Gd Tb Dy Ho Er Tm Yb Lu
100
10
1
.1
PICH 158
PICH 66D
Amphibole
Plagioclase
Pyroxene

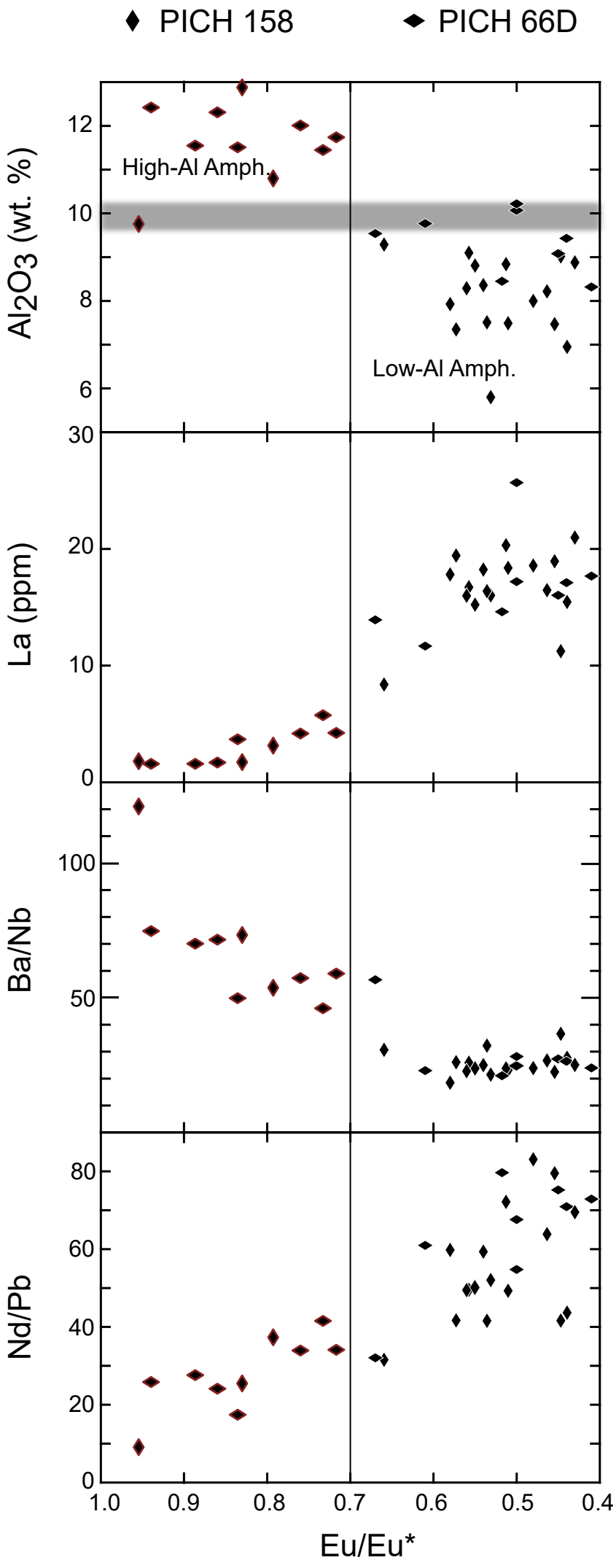
PICH 158
PICH 66D
High-Al Amph.
Low-Al Amph.
Al2O3 (wt. %)
La (ppm)
Ba/Nb
Nd/Pb
Eu/Eu*
12
10
8
6
30
20
10
0
100
50
80
60
40
20
0
1.0
0.9
0.8
0.7
0.6
0.5
0.4

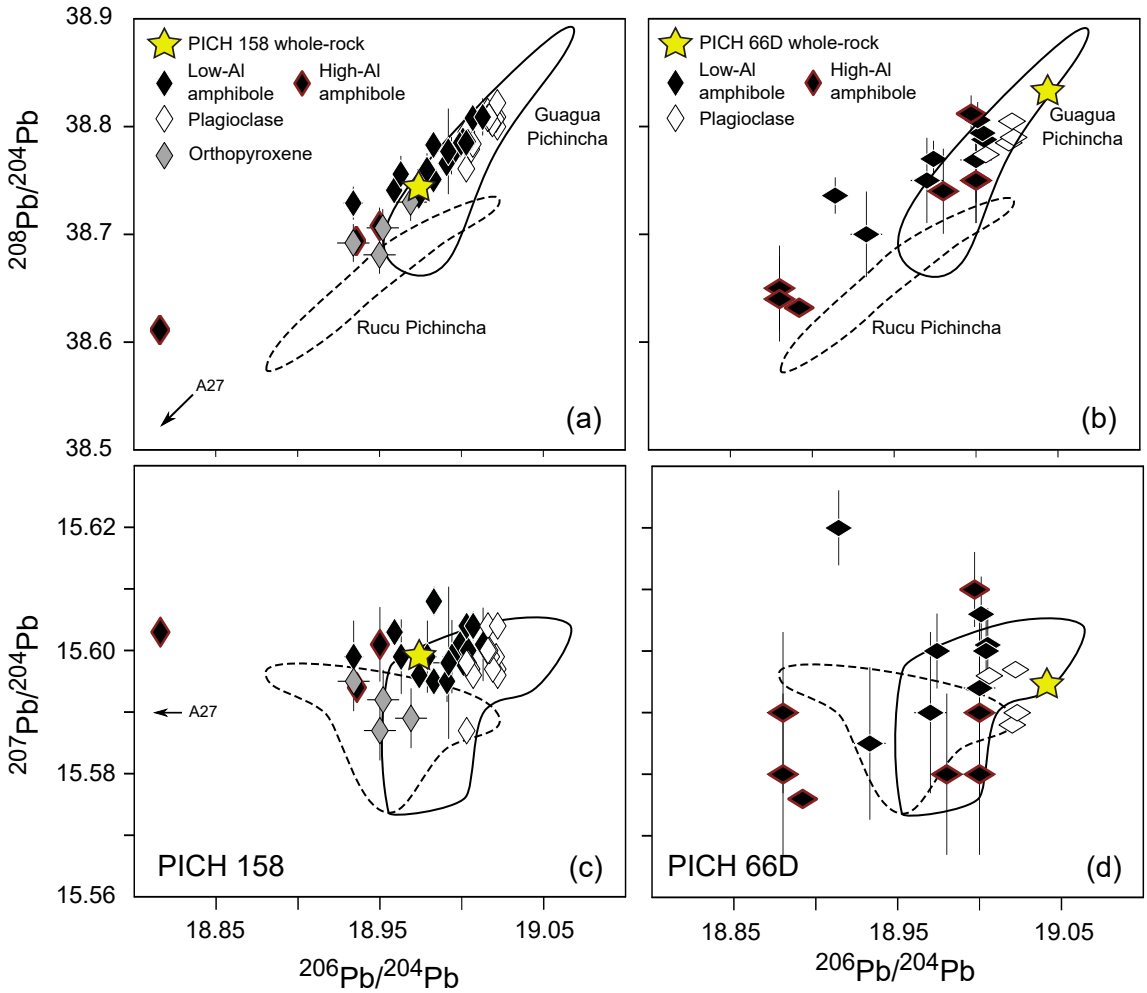
PICH 158 whole-rock
Low-Al amphibole
High-Al amphibole
Plagioclase
Orthopyroxene
Guagua Pichincha
Rucu Pichincha
A27
(a)
PICH 66D whole-rock
Low-Al amphibole
High-Al amphibole
Plagioclase
Guagua Pichincha
Rucu Pichincha
(b)
A27
PICH 158
(c)
PICH 66D
(d)
38.9
38.8
38.7
38.6
38.5
15.62
15.60
15.58
15.56
18.85
18.95
19.05
$^{208}Pb/^{204}Pb$
$^{207}Pb/^{204}Pb$
$^{206}Pb/^{204}Pb$

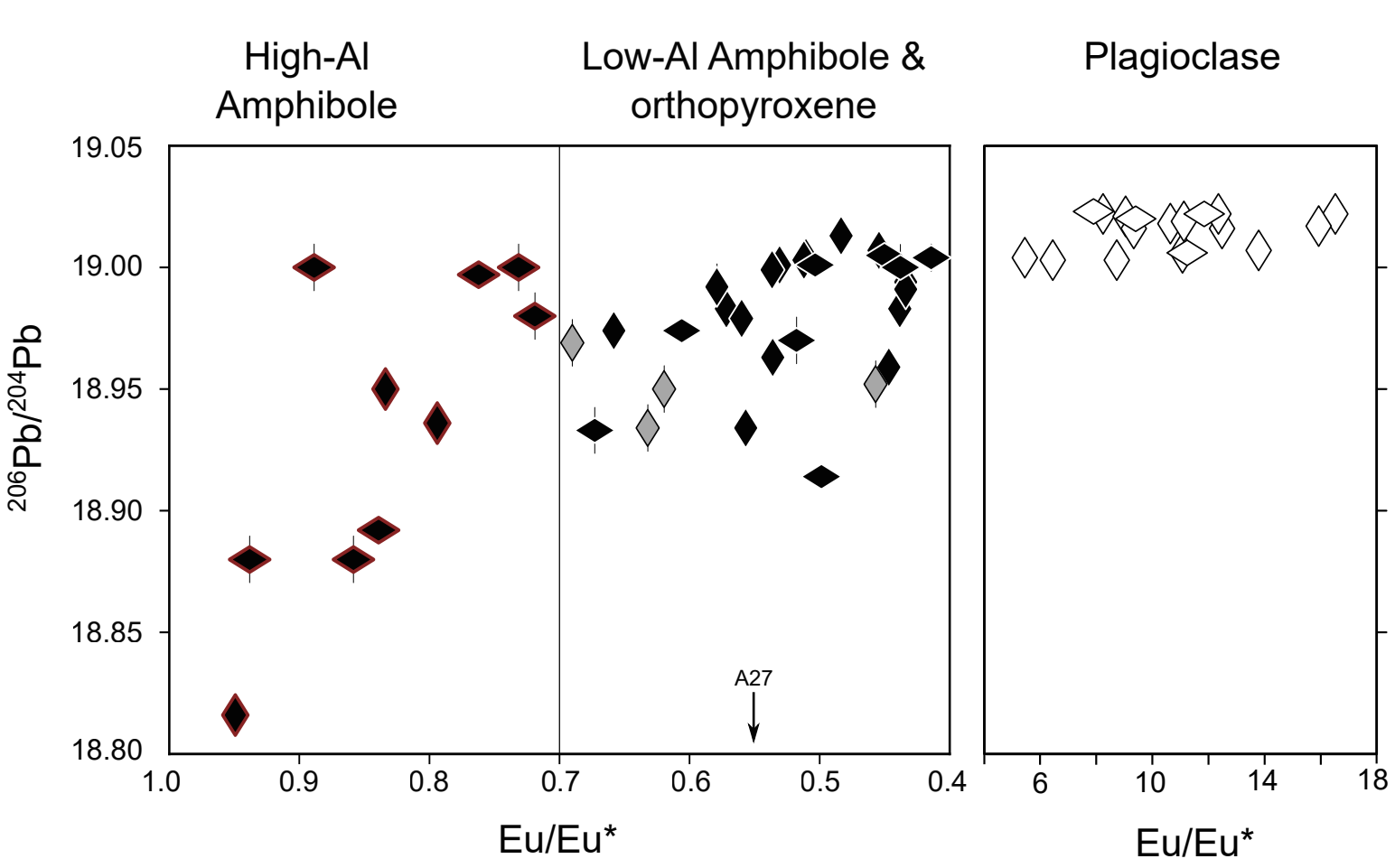
High-Al Amphibole
Low-Al Amphibole & orthopyroxene
Plagioclase
19.05
19.00
18.95
18.90
18.85
18.80
$^{206}Pb/^{204}Pb$
A27
1.0
0.9
0.8
0.7
0.6
0.5
0.4
6
10
14
18
Eu/Eu*
Eu/Eu*

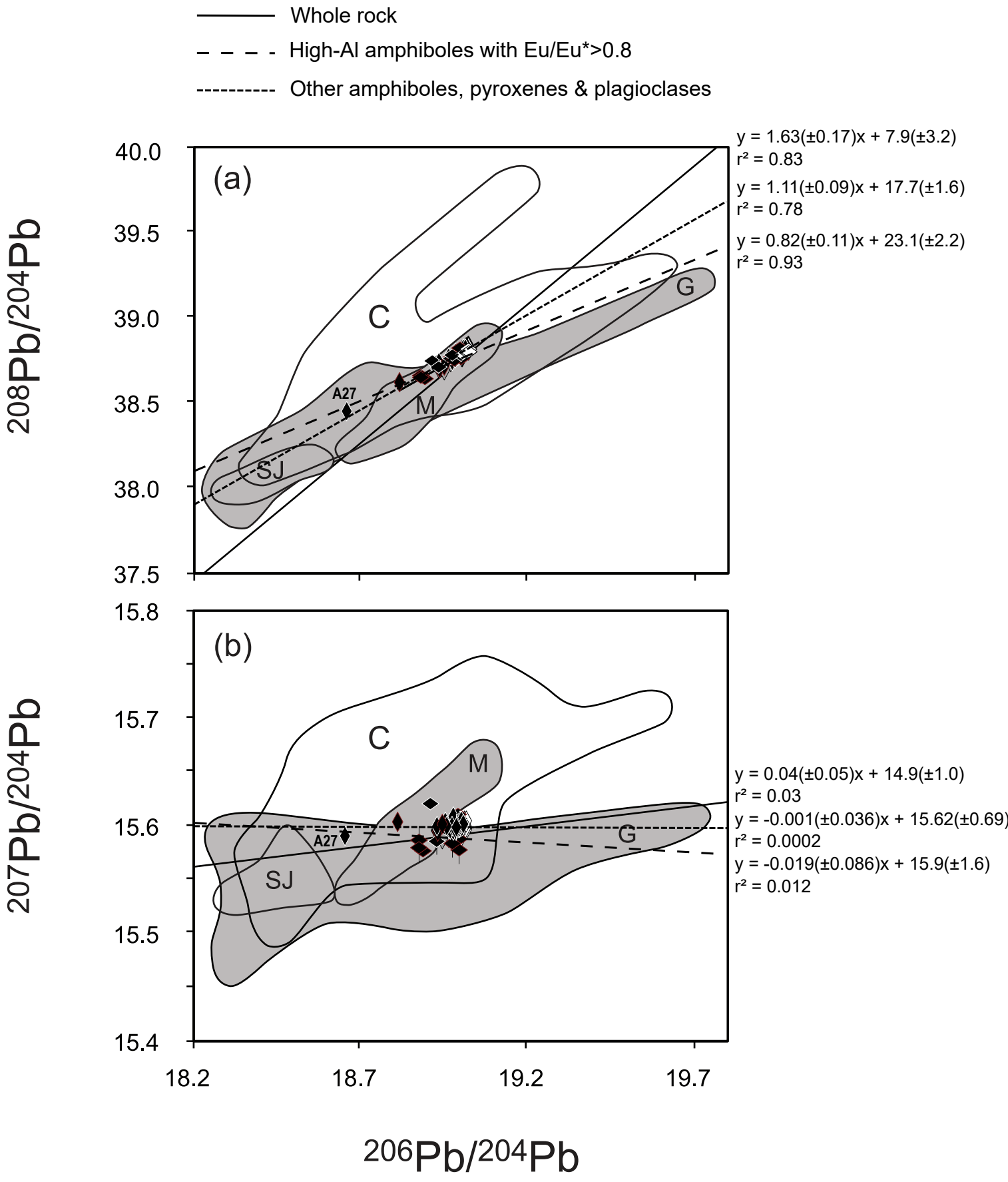
Whole rock
High-Al amphiboles with Eu/Eu*>0.8
Other amphiboles, pyroxenes & plagioclases
(a)
(b)
C
M
G
SJ
A27
y = 1.63(±0.17)x + 7.9(±3.2)
r² = 0.83
y = 1.11(±0.09)x + 17.7(±1.6)
r² = 0.78
y = 0.82(±0.11)x + 23.1(±2.2)
r² = 0.93
y = 0.04(±0.05)x + 14.9(±1.0)
r² = 0.03
y = -0.001(±0.036)x + 15.62(±0.69)
r² = 0.0002
y = -0.019(±0.086)x + 15.9(±1.6)
r² = 0.012
40.0
39.5
39.0
38.5
38.0
37.5
15.8
15.7
15.6
15.5
15.4
18.2
18.7
19.2
19.7
208Pb/204Pb
207Pb/204Pb
206Pb/204Pb

Fig.7

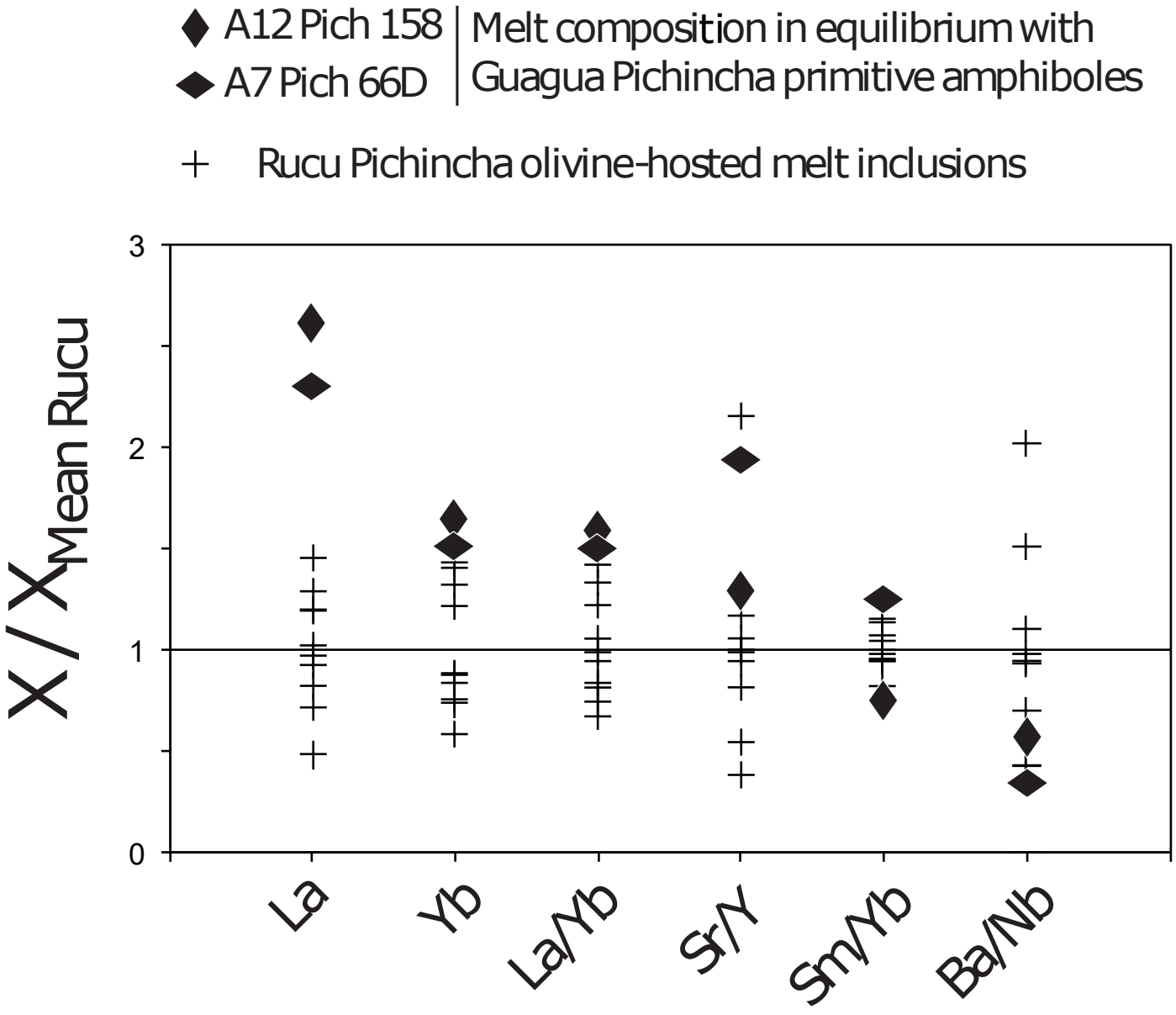
A12 Pich 158
A7 Pich 66D
Melt composition in equilibrium with Guagua Pichincha primitive amphiboles
Rucu Pichincha olivine-hosted melt inclusions
X / X Mean Rucu
3
2
1
0
La
Yb
La/Yb
Sr/Y
Sm/Yb
Ba/Nb

Table 1: Pb isotope compositions of whole rocks and separate minerals

Sample/phase		Lead extracted (ng)	Blank content (pg)	$^{206}Pb/^{204}Pb$	2SE	2SD	$^{207}Pb/^{204}Pb$	2SE	2SD	$^{208}Pb/^{204}Pb$	2SE	2SD	Eu/Eu*	Al_2O_3
PICH 158														
Whole rock				18,9740			15,5990			38,7450			0,99	
Groundmass**				18,9704			15,5990			38,7401				
Amphibole	**A1 Pich 158**	1,83	21,4	18,936	0,0012	0,0018	15,594	0,0011	0,0018	38,694	0,0028	0,0049	0,79	10,8
	A2 Pich 158	7,18	21,4	18,959	0,0012	0,0018	15,603	0,0011	0,0018	38,741	0,0030	0,0049	0,45	9,02
	A2 Pich 158 R	/	/	18,958	0,0010	0,0018	15,602	0,0009	0,0018	38,739	0,0022	0,0049	/	/
	A3 Pich 158	4,3	21,4	18,983	0,0011	0,0018	15,595	0,0010	0,0018	38,751	0,0023	0,0049	0,57	7,35
	A4 Pich 158	5,94	21,4	19,001	0,0010	0,0018	15,598	0,0010	0,0018	38,787	0,0023	0,0049	0,53	5,80
	A4 Pich 158 R	/	/	19,002	0,0012	0,0018	15,599	0,0010	0,0018	38,788	0,0026	0,0049	/	/
	A5 Pich 158	4,59	21,4	18,999	0,0012	0,0018	15,601	0,0010	0,0018	38,783	0,0025	0,0049	0,54	7,51
	A6 Pich 158	5,88	21,4	19,004	0,0011	0,0018	15,600	0,0010	0,0018	38,786	0,0025	0,0049	0,51	7,49
	A7 Pich 158	3,35	21,4	19,003	0,0011	0,0018	15,604	0,0010	0,0018	38,785	0,0025	0,0049	0,51	8,84
	A8 Pich 158	2,71	21,4	18,974	0,0011	0,0018	15,596	0,0010	0,0018	38,736	0,0024	0,0049	0,66	9,29
	A10 Pich 158	7,66	8,4	18,983	0,0020	0,0018	15,608	0,0017	0,0023	38,783	0,0042	0,0067	0,44	6,95
	A12 Pich 158	3,94	8,4	18,816	0,0028	0,0018	15,603	0,0024	0,0023	38,611	0,0062	0,0067	0,95	9,76
	A19 Pich 158	0,93	8,4	18,934	0,0050	0,0056	15,599	0,0042	0,0058	38,729	0,0110	0,0148	0,56	9,10
	A20 Pich 158	0,92	8,4	18,979	0,0022	0,0056	15,599	0,0019	0,0058	38,760	0,0048	0,0148	0,56	8,29
	A21 Pich 158	2,44	8,4	19,007	0,0029	0,0018	15,604	0,0024	0,0023	38,808	0,0062	0,0067	0,45	7,47
	A22 Pich158*	2,64	19,5	18,994	0,0014	0,0056	15,599	0,0010	0,0059	38,773	0,0026	0,0168	0,43	8,88
	A22 Pich158 R*	/	/	18,991	0,0012	0,0033	15,595	0,0011	0,0033	38,766	0,0024	0,0076	/	/
	A23 Pich158*	1,41	19,5	19,013	0,0012	0,0056	15,601	0,0011	0,0059	38,809	0,0026	0,0168	0,48	8,00
	A24 Pich 158*	0,42	19,5	18,963	0,0025	0,0049	15,599	0,0021	0,0060	38,756	0,0050	0,0163	0,54	8,36
	A25 Pich158*	0,83	19,5	18,992	0,0019	0,0094	15,598	0,0018	0,0123	38,777	0,0045	0,0392	0,58	7,93
	A26 Pich158*	0,25	19,5	18,950	0,0043	0,0049	15,601	0,0038	0,0060	38,708	0,0089	0,0163	0,83	12,88
	A27 Pich158*	0,41	19,5	18,658	0,0025	0,0049	15,590	0,0020	0,0060	38,441	0,0050	0,0163	0,55	8,81
Orthopyroxene	**Px 6 Pich 158**	0,45	4,5	18,952	0,0062	0,0096	15,592	0,0051	0,0048	38,706	0,0123	0,017	0,46	
	Px 7 Pich 158	0,15	4,5	18,970	0,0076	0,0096	15,589	0,0065	0,0048	38,730	0,0164	0,017	0,69	
	Px 9 Pich 158	0,25	4,5	18,935	0,0049	0,0096	15,595	0,0045	0,0048	38,693	0,0103	0,017	0,63	
	Px 14 Pich 158	0,29	4,5	18,950	0,0086	0,0096	15,587	0,0070	0,0048	38,682	0,0182	0,017	0,62	
Plagioclase	**Pl 1 Pich 158**	15,01	9,8	19,022	0,0010	0,0011	15,597	0,0008	0,0013	38,809	0,0020	0,0038	8,24	
	Pl 1 Pich 158 R	/	/	19,027	0,0056	0,0011	15,601	0,0047	0,0013	38,821	0,0118	0,0038	/	
	Pl 3 Pich 158	10,61	9,8	19,003	0,0011	0,0011	15,598	0,0009	0,0013	38,795	0,0024	0,0038	8,73	
	Pl 4 Pich 158	17,91	9,8	19,022	0,0009	0,0011	15,596	0,0007	0,0013	38,800	0,0022	0,0038	16,52	
	Pl 5 Pich 158	11,38	9,8	19,004	0,0009	0,0011	15,598	0,0008	0,0013	38,782	0,0020	0,0038	5,44	
	Pl 6 Pich 158	15,3	9,8	19,021	0,0008	0,0011	15,599	0,0007	0,0013	38,807	0,0017	0,0038	9,05	
	Pl 7 Pich 158	8,6	9,8	19,018	0,0009	0,0011	15,599	0,0008	0,0013	38,805	0,0022	0,0038	10,64	
	Pl 8 Pich 158	21,88	9,8	19,006	0,0010	0,0011	15,597	0,0008	0,0013	38,779	0,0022	0,0038	11,07	
	Pl 9 Pich 158	11,42	9,8	19,016	0,0010	0,0011	15,604	0,0008	0,0013	38,814	0,0028	0,0038	9,33	
	Pl 10 Pich 158	12,54	9,8	19,019	0,0011	0,0011	15,597	0,0009	0,0013	38,803	0,0025	0,0038	11,11	
	Pl 10 Pich 158 R	/	/	19,019	0,0010	0,0011	15,597	0,0008	0,0012	38,803	0,0022	0,0031	/	
	Pl 11 Pich 158	4,37	4,7	19,003	0,0009	0,0013	15,587	0,0008	0,0013	38,761	0,0021	0,0038	6,44	25,2
	Pl 12 Pich 158	4,69	4,7	19,007	0,0008	0,0013	15,596	0,0007	0,0013	38,784	0,0019	0,0033	13,81	25,6
	Pl 14 Pich 158	2,63	4,7	19,016	0,0013	0,0013	15,600	0,0012	0,0013	38,808	0,0030	0,0033	12,47	24,1
	Pl 15 Pich 158	2,12	4,7	19,022	0,0022	0,0013	15,604	0,0018	0,0013	38,822	0,0047	0,0033	12,37	25,8
	Pl 16 Pich 158	6,49	4,7	19,017	0,0017	0,0013	15,600	0,0015	0,0013	38,809	0,0037	0,0033	15,90	25,1
PICH 66D														
Whole rock				19,0426			15,5945			38,8326			0,96	
Groundmass**				19,0440			15,5946			38,8348				
Amphibole	**A1 Pich 66D**	0,73	10,8	18,999	0,0067	0,0096	15,587	0,0058	0,013	38,754	0,0145	0,039	0,89	11,5
	A2 Pich 66D	1,13	10,8	18,892	0,0018	0,0010	15,576	0,0016	0,0012	38,632	0,0022	0,0035	0,84	11,5
	A3 Pich 66D	0,7	10,8	18,999	0,0034	0,0096	15,577	0,0030	0,013	38,755	0,0080	0,039	0,73	11,5
	A4 Pich 66D	0,35	10,8	18,971	0,0067	0,0096	15,594	0,0057	0,013	38,753	0,0148	0,039	0,52	8,45
	A6 Pich 66D	0,29	10,8	18,980	0,0063	0,0096	15,583	0,0053	0,013	38,746	0,0141	0,039	0,72	11,7
	A7 Pich 66D	0,18	10,8	18,879	0,0092	0,0096	15,586	0,0074	0,013	38,648	0,0194	0,039	0,94	12,4
	A8 Pich 66D	0,18	10,8	18,880	0,0117	0,0096	15,579	0,0083	0,013	38,639	0,0218	0,039	0,86	12,3
	A9 Pich66D*	1,21	19,5	19,005	0,0014	0,0056	15,601	0,0012	0,0059	38,788	0,0029	0,0168	0,45	9,1
	A10 Pich66D*	0,77	19,5	19,000	0,0017	0,0094	15,594	0,0015	0,0123	38,769	0,0038	0,0392	0,44	9,4
	A11 Pich 66D*	1,05	19,5	19,004	0,0015	0,0056	15,600	0,0013	0,0059	38,794	0,0030	0,0168	0,41	8,3
	A12-1 Pich66D*	0,27	19,5	19,001	0,0031	0,0049	15,606	0,0025	0,0060	38,806	0,0065	0,0163	0,50	10,1
	A12-2 Pich66D*	0,28	19,5	18,914	0,0031	0,0049	15,620	0,0025	0,0060	38,736	0,0064	0,0163	0,50	10,2
	A13 Pich66D*	0,26	19,5	18,974	0,0040	0,0049	15,600	0,0032	0,0060	38,770	0,0083	0,0163	0,61	9,8
	A14 Pich66D*	0,72	19,5	18,933	0,0023	0,0094	15,585	0,0020	0,0123	38,700	0,0048	0,0392	0,67	9,5
	A15 Pich66D*	0,25	19,5	18,997	0,0037	0,0049	15,610	0,0029	0,0060	38,812	0,0079	0,0163	0,76	12,0
Plagioclase	**Pl 1 Pich 66D**	8,92	10,8	19,006	0,0009	0,0010	15,596	0,0009	0,0012	38,774	0,0022	0,0035	11,25	22,9
	Pl 2 Pich 66D	6,73	10,8	19,020	0,0012	0,0010	15,588	0,0010	0,0012	38,785	0,0026	0,0035	9,42	24,6
	Pl 3 Pich 66D	12,15	10,8	19,022	0,0010	0,0010	15,597	0,0008	0,0012	38,805	0,0020	0,0035	11,81	21,7
	Pl 4 Pich 66D	3,68	10,8	19,023	0,0014	0,0010	15,590	0,0012	0,0012	38,790	0,0023	0,0035	7,89	24,6

Pb isotopic compositions are normalized to the NBS981 values of Todt et al. (1996)
2SE = in-run 2 standard error
2SD = 2 standard deviation of the analysis session, calculated through NBS 981 standards repeatibility
* set of sample for which the Tl could not be used for mass fractionation correction, the mass fractionation was corrected externally by standard bracketing
** Groundmass composition is calculated by mass balance (see text)
Al_2O_3 contents are not displayed for leached samples
Sample named R are replicates